Aalto-yliopisto
Insinööritieteiden
korkeakoulu

Laura Sirkiä

Applicability of miniature Compact Tension specimens for fracture toughness determination in ductile-brittle transition range

Thesis submitted in partial fulfilment of the requirements
for the degree of Master of Science in Technology.

Espoo 17.11.2017

Supervisor: Professor Hannu Hänninen

Advisor: Sebastian Lindqvist, M.Sc. (Tech.)

Aalto-yliopisto
Insinööritieteiden
korkeakoulu

Aalto-yliopisto, PL 11000, 00076 AALTO
www.aalto.fi

Diplomityön tiivistelmä

Tekijä Laura Sirkiä

Työn nimi Minikokoisten Compact Tension sauvojen käytettävyys murtumissitkeyden määrittämiseen sitkeä-hauras transitioalueella

Koulutusohjelma Konetekniikka

Pääaine Koneenrakennuksen materiaalitekniikka **Koodi** K3003

Työn valvoja Professori Hannu Hänninen

Työn ohjaaja Diplomi-insinööri Sebastian Lindqvist

Päivämäärä 17.11.2017 **Sivumäärä** 80 **Kieli** Englanti

Tiivistelmä

Säteilyseuranta-ohjelma (surveillance) perustettiin ydinvoimalaitoksissa (YVL) käytössä olevien reaktoripaineastioiden (RPV) kunnon valvomiseksi. Bainiittis-ferriitisten paineastiaterästen säännöllinen testaaminen on välttämätöntä, koska säteily huonontaa mekaanisia ominaisuuksia ja nostaa tilakeskisen kuutiollisen (TKK) teräksen transitiolämpötilaa sitkeä-hauras alueella. Pääasiallisesti säteilyseuranta ohjelman iskukokeet suoritetaan Charpy-V (CVN) sauvoilla. Testatuista CVN sauvan puolikkaista voidaan valmistaa minikokoisia Compact Tension (C(T)) sauvoja.

Minikokoisten C(T) sauvojen käyttö murtumissitkeyden määrittämiseen sitkeä-hauras transitioalueella on suuren mielenkiinnon kohde YVL tekniikassa ja sitä tutkitaan tässä työssä. Tämän hetkinen tietämys minikokoisten sauvojen käytettävyydestä on epävarmaa, sillä koesauvan pienempi koko saattaa antaa liian suuria murtumissitkeysarvoja.

Kahta materiaalia tutkittiin transitiolämpötilan T_0 määrittämiseksi. Barsebäck 2 materiaalia ja Ringhals 4 varahitsiainetta. Murtumismekaniikan käsitteet ja yleiskuvaus RPV materiaaleista sekä valmistusmetodeista esitetään pääpiirteittäin kirjallisuuskatsauksessa. Murtumissitkeyskokeet tehtiin yhdessä murtopintojen karakterisoinnin ja kovuusmittausten kanssa. Mikrorakennetarkasteluissa ilmeni, että mini C(T) sauvat sijaitsivat hitsiaineessa, muutosvyöhykkeessä sekä perusmateriaalissa, ja siitä johtuen nimitys tarkentui Barsebäck 2 materiaaliksi.

Määritetyt transitiolämpötilat T_0 olivat: Barsebäck 2 materiaali, -99 °C ja Ringhals 4 varahitsiaine, -68 °C. Barsebäck 2 materiaalin tuloksia verrattiin olemassa oleviin samankaltaisen kemiallisen koostumuksen terästen Master Curve tuloksiin Ringhals 3 ja Ringhals 4 laitoksista. Tässä työssä saatu T_0 oli samalla alueella koesauvan pienestä koosta huolimatta. Näin ollen, minikokoinen C(T) sauva antaa koosta riippumattoman T_0 arvon ja minisauvakoon käyttäminen on mahdollista materiaalille.

Avainsanat reaktoripaineastia, säteilyseuranta ohjelma, sitkeä-hauras transitioalue, haurasmurtuma, mini C(T) sauva, transitiolämpötila T_0, hitsiaine

Aalto University
School of Engineering
Aalto University, P.O.BOX 11000,00076 AALTO
www.aalto.fi

Abstract of master's thesis

Author Laura Sirkiä

Title of thesis Applicability of miniature Compact Tension specimens for fracture toughness determination in ductile-brittle transition range

Degree programme Mechanical Engineering

Major Engineering Materials **Code** K3003

Thesis supervisor Professor Hannu Hänninen

Thesis advisor Sebastian Lindqvist, M.Sc. (Tech.)

Date 17.11.2017 **Number of pages** 80 **Language** English

Abstract

Surveillance programs were established to monitor reactor pressure vessels (RPV) in service of nuclear power plants (NPP). Regular testing of bainite-ferrite RPV steel is essential, since irradiation is known to cause degradation in mechanical properties as well as rising of the ductile-brittle transition temperature of body-centred cubic (bcc) steels. Surveillance impact testing is mainly performed with Charpy-V notch (CVN) specimens. The tested CVN specimen halves are feasible for manufacturing of miniature size Compact Tension (C(T)) specimens.

The usage of miniature size C(T) specimens for determination of fracture toughness in ductile-brittle transition range is of great interest in NPP field and it is studied in this thesis. Present knowledge of applicability of sub-size specimens is somewhat uncertain considering that reduced specimen size may give increased fracture toughness values.

Two types of materials were examined. Barsebäck 2 material and Ringhals 4 surrogate weld metal in order to determinate the transition temperature T_0. Characteristics of fracture mechanics and an overview of RPV materials and methods were outlined in the literature. Fracture toughness tests were carried out together with fractographic characterization and hardness measurements. Microstructural examinations revealed that the miniature C(T) specimens located in the weld metal, HAZ and base material, and is therefore referred to as Barsebäck 2 material hereafter.

The determined transition temperatures T_0 of Barsebäck 2 material and Ringhals 4 surrogate weld metal were: B2, -99°C and R4, -68°C. The Barsebäck 2 material results of this thesis were compared to the existing results from Master Curve testing of the Ringhals 3 and Ringhals 4 NPP steels, with similar chemistry. The determined T_0 of this thesis was in the same range, despite of the smaller specimen size. Consequently, the miniature C(T) specimens give a size independent T_0 value and the applicability of the specimen configuration is possible for the material.

Keywords RPV, surveillance program, ductile-brittle transition, cleavage fracture, miniature C(T) specimen, transition temperature T_0, weld metal

Preface

This thesis is a part of LOST project, a sub-project of the Finnish Nuclear Power Plant Safety 2014-2018 programme (SAFIR2018) and was carried out at VTT Technical Research Centre of Finland. The work is also part of BREDA project, a Finnish-Swedish collaboration project related to the Barsebäck 2 nuclear power plant.

The studied materials in this thesis, Barsebäck 2 material and Ringhals 4 surrogate weld metal were delivered through courtesy of Pål Efsing from Ringhals/Vattenfall, which is greatly acknowledged.

I want to thank my supervisor, Professor Hannu Hänninen, from constructive feedback as well as suggestive discussions with a twist of humour. I am grateful to Sebastian Lindqvist, my thesis advisor; you always had the time for my questions; even for the tiring ones. Your opinions and proficiency were beyond comparison.

Colleagues from VTT; Tommi Seppänen, Marketta Mattila, Jari Lydman and a former colleague Esa Varis, thank you for valuable expertise and support. As well as to all others who helped me during the thesis process.

Last, but definitely not least, a very big hug to my own family! I am through with the writing now. Thank you for your patience.

Espoo 17.11.2017

Laura Sirkiä

Table of Contents

List of abbreviations and symbols

a	crack length
a/W	crack aspect ratio
a_0	initial crack length
ASME	American Society of Mechanical Engineers
ASTM	American Society for Testing and Materials
B	specimen thickness
B_N	net thickness of side-grooved specimen
bcc	body-centred cubic
BWR	boiling water reactor
CVN	Charpy-V notch specimen
COD	crack-opening displacement
C(T)	compact tension specimen
CTOD	crack-tip-opening displacement
f(a/W)	a dimensionless function that reflects the geometry and mode of loading of the specimen
fcc	face-centred cubic
G	grain size index
HAZ	heat-affected zone
IIW	International Institution of Welding
J	J-integral, used to characterize the local stress-strain field around the crack front
J_e	elastic component of J
J_p	plastic component of J
J-R curve	a plot of crack extension resistance as a function of stable crack extension
K	stress intensity factor
K_C	fracture toughness
K_{Jc}	fracture toughness determined by conversion from J
$K_{Jc(B)}$	K_{Jc} for a specimen size B
$K_{Jc(i)}$	either a valid K_{Jc} or censored value
$K_{Jc(med)}$	the median of a K_{Jc} data
$K_{Jc(1T)}$	K_{Jc} for a specimen size 1T
K_{min}	threshold toughness
K_0	a K_{Jc} value that represents the 63 percentile level of a K_{Jc} data distribution
LEFM	linear elastic fracture mechanics
m	constraint factor, number of grains per square millimetre
N	number of specimen tested
NPP	nuclear power plants
P	load
PWR	pressurized water reactor
RPV	reactor pressure vessel
S	span
SE(B)	single-edge bend specimen
T	test temperature
T_i	test temperature corresponding to $K_{Jc(i)}$
T_0	transition temperature
T_{0Q}	provisional T_0 value

TEM	transmission electron microscopy
W	specimen width
Y	a constant related to specimens geometry
Δa	crack extension
Δa_p	slow stable crack growth
δ	crack-tip-opening displacement
δ_i	Kronecker delta; either one (test ended with cleavage fracture) or zero (test ended with ductile fracture mode)
σ_C	critical stress for crack propagation
σ_f	critical fracture stress/failure stress
σ_{TS}	ultimate tensile strength
σ_{YS}	yield strength
σ_{yy}	stress component in *y* direction, perpendicular to crack plane
φ	twist angle
ψ	tilt angle

1 Introduction

In nuclear power plants (NPP), the most critical component is the reactor pressure vessel (RPV) containing the reactor core. The RPV is a colossal structure and due to its size, it is manufactured by welding from forged individual parts. Dimensions typically are: height 12-14 m, inner diameter 4-5 m, wall thickness 20 cm and over, and weight ca 500 000 kg.

Figure 1 represents a version of a typical reactor vessel. On the upper part of the RPV a control rod drive mechanism is located, whereas fuel rods are located in the reactor core at lower part of the RVP and in the middle part outside the RPV are the locations of main pump line outputs. Figure 2 demonstrates segments of the RPV. The RPV top cap including a head flange is manufactured as a separate component from the vessel and is attached to the RPV at mounting stage at the site of the nuclear power plant.

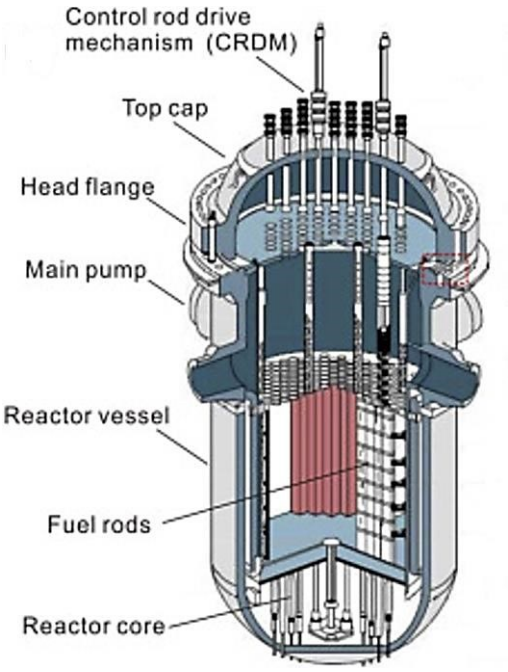

Figure 1 Cutaway of a typical RPV. (Shen et al., 2016)

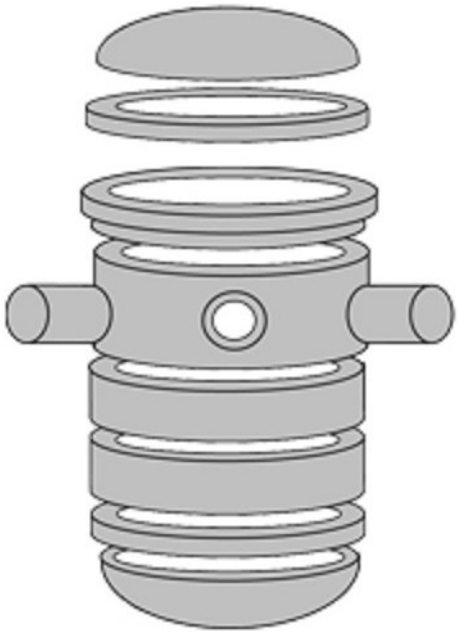

Figure 2 RPV consists of individual forged sections welded together. (American Nuclear Society, 2012)

The RPV usually specifies safety in service since change of the RPV is not an option for technical and financial reasons (Haušild et al., 2016). Manufacturing of the RPV is extremely costly and it is nearly unfeasible to reproduce the RPV within similar dimensions. Hence, the RPV is under constant surveillance.

The RPV is made from bainite-ferrite steel; precisely with lower bainite because of its required higher strength and higher toughness properties as compared to upper bainite. Moreover, bainite-ferrite steels can be produced without expensive heat treatment processes (Campbell, 2008). Bainite-ferrite steel has excellent features such as good toughness, is suitable for welding and cheaper than austenitic steel. In addition, bainite-ferrite steel has more resistance to irradiation-induced swelling than austenitic steel (Blagoeva et al., 2014). Nevertheless, bainite-ferrite steel has a tendency to brittle

behaviour. Bainite-ferrite steel has a bcc crystal structure whereas austenitic steel has an fcc crystal structure. Therefore at certain conditions, such as under irradiation or at low temperatures, the bcc steel has an increasing tendency to brittle behaviour.

Embrittlement caused by irradiation is a severe challenge in nuclear conditions for ferritic steels. The RPV material is under constant neutron flux and thereby material hardens. Over time it induces degradation of mechanical properties of the RPV, especially in toughness. (Soneda, 2015)

In addition, irradiation causes rising of the ductile-brittle transition temperature. Below certain temperature, material is brittle and above it, the material is ductile. Between them locates a ductile-to-brittle transition range, where the material is neither brittle nor ductile. In Figure 3 is a schematic view how irradiation shifts the transition curve to higher temperature. Consequently, the material that used to be ductile becomes now brittle caused by irradiation. This time-dependent degradation process causes safety issues for NPPs and creates a need for long-term surveillance.

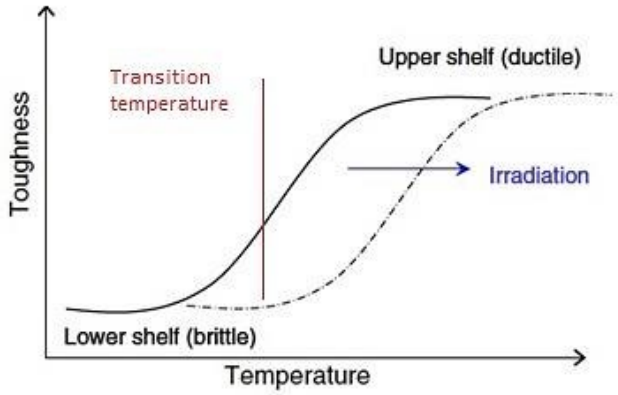

Figure 3 Shift of transition curve caused by irradiation. (Chen et al., 2007)

NPPs have a limited, licensed lifetime. To control operating of nuclear RPVs, surveillance programs are established. Initially surveillance programs were planned for 40 years of lifetime and at present there are several NPPs having an extended license for 60 years. Even 80 years of lifetime is scheduled (Server et al., 2017). Furthermore, particularly the fact that radiation-induced embrittlement was occurring at a higher rate than anticipated influenced to the establishment of surveillance programs. (Hertzberg et al., 2013)

The intention of surveillance programs is to observe changes in the mechanical properties such as strength and toughness in life-limiting structural materials caused by irradiation. To get data of possible changes a reference material is needed. Figure 4 clarifies where capsules containing reference specimens are located; between an inner wall of RPV and the reactor core. From the test data is obtained an early estimate for any decays of properties. (AREVA, 2017; English & Hyde, 2012)

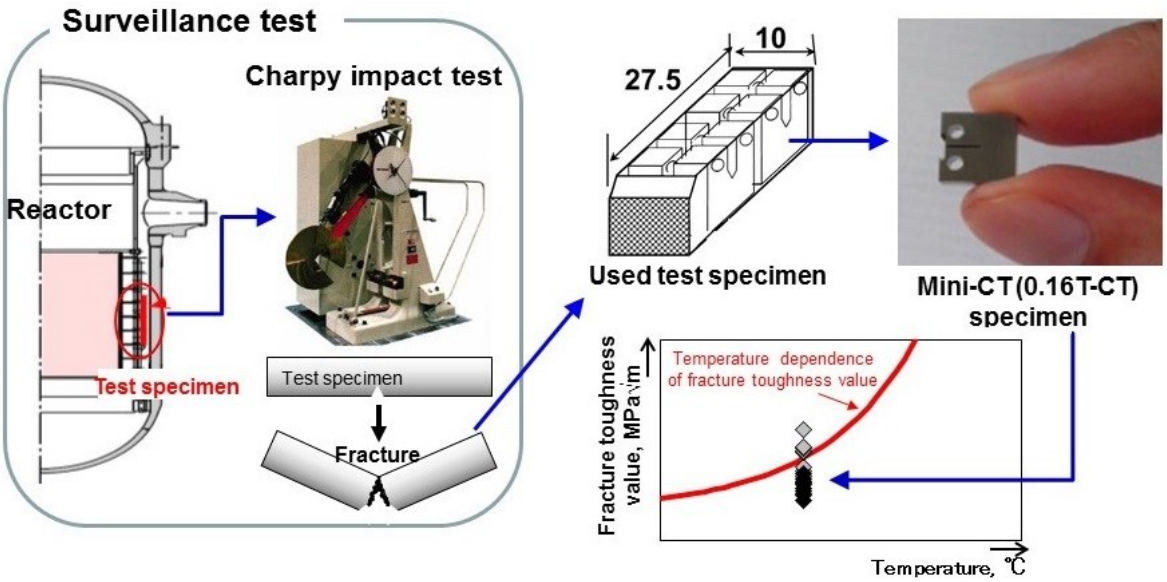

Figure 4 Cycle of RPV surveillance program.
(Japan Atomic Energy Agency)

There is only a limited amount of valuable representative materials available. In surveillance programs impact tests are performed with Charpy-V notch (CVN) specimens using a pendulum as the impact test machine. Figure 5 gives an idea of how the impact test is made. The CVN specimen is placed on the anvil of the machine, notch side away from the hammer, and the hammerhead swings freely impacting the CVN specimen. Dimensions of the CVN specimen are usually 10x10x55 mm. The tested CVN specimen halves are still usable and can be exploited, in this case, for miniature size C(T) specimens. Figure 4 explains the surveillance cycle and utilization of the tested specimen halves.

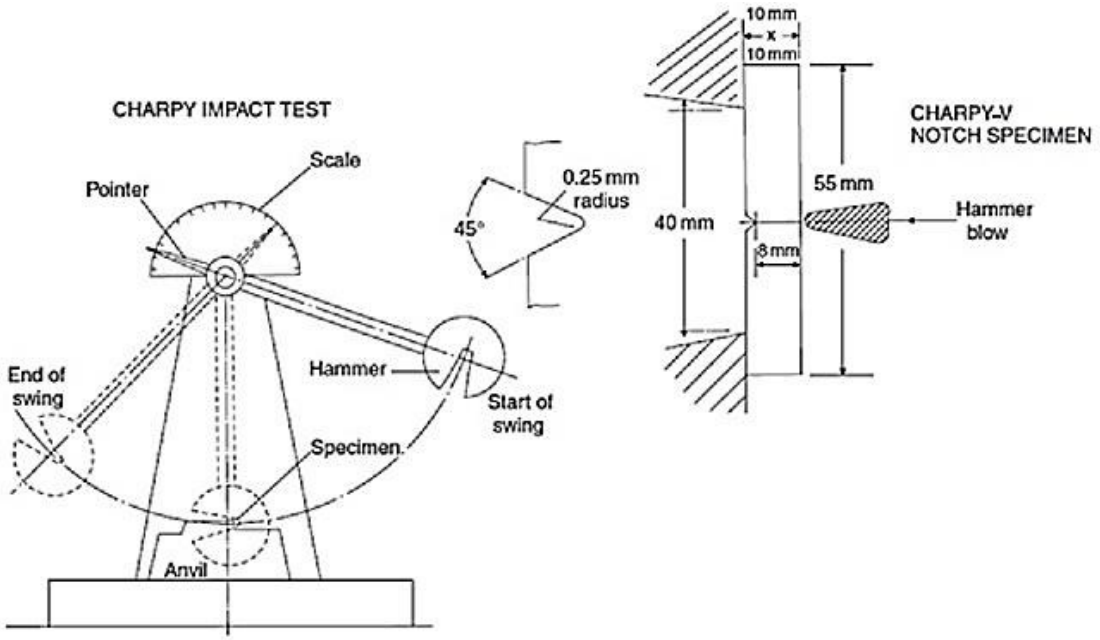

Figure 5 Impact test machine and Charpy-V notch specimen
(Eyres and Bruce, 2012)

Research has been done exploiting surveillance tested CVN halves for feasibility of miniature size compact tension C(T) specimens. Thus far research has mainly related to validating homogeneous material, less of weld metal. In addition, fracture toughness can be size dependent and hence, the applicability of sub-size specimens is yet uncertain.

The aim of this thesis is not only to study the usability of miniature size C(T) specimens but also to research the reliability of the test results received from testing of weld metals.

At the beginning ductile-brittle transition range, with ductile and brittle crack growths, including embrittlement, are presented. It is followed by the Master Curve theory and a brief introduction from fracture mechanics concept. An overall of RPV materials and manufacturing, and materials of this thesis with manufacturing of miniature specimens are portrayed as well as a description of two fracture toughness testing procedures which are based on the American Society for Testing Materials (ASTM) E1820 'Standard Test Method for Measurement of Fracture Toughness' and ASTM E1921 'Standard Test Method for Determination of Reference Temperature, T_0, for Ferritic Steels in the Transition Range' are outlined.

Moreover, metallographic characterisation and the experimental research are demonstrated. The results including hardness, initial crack size, and characterisation of the fracture surface and microstructure with determination of the transition temperature T_0 are introduced. Thesis is concluded with discussion of the results and conclusions.

2 Theory

The theory part clarifies the transition range phenomena and explains differences between ductile fracture and brittle, cleavage fracture followed by a presentation of embrittlement caused by irradiation. The Master Curve theory, a brief introduction of fracture mechanics concept with standard ASTM E1820 as well as description of RPV materials and manufacturing are introduced.

2.1 Transition range

A range between ductile fracture and brittle fracture is termed as the transition range. The fracture toughness of ferritic steels, in consequence of the bcc microstructure, depends from the temperature. At different temperatures fracture modes are diverse; near the lower shelf at low temperatures the fracture occurs by cleavage initiation, whereas above the transition range, in the upper shelf, fracture converts to fully ductile fracture (Planman and Server, 2012). Transition range is presented in Figure 6. Metals with bcc microstructure do have strong yield strength-temperature sensitivity. (Hertzberg et al., 2013)

Numerous factors may influence to the ductile-to-brittle transition temperature, such as grain size, crystal structure and second-phase particles, for instance. Transition temperature decreases with the reduction of the ferrite grain size, regardless of the fact that the yield strength increases. Furthermore, second-phase particles may cause cleavage cracks to initiate leading to fracture. (Krauss, 2015)

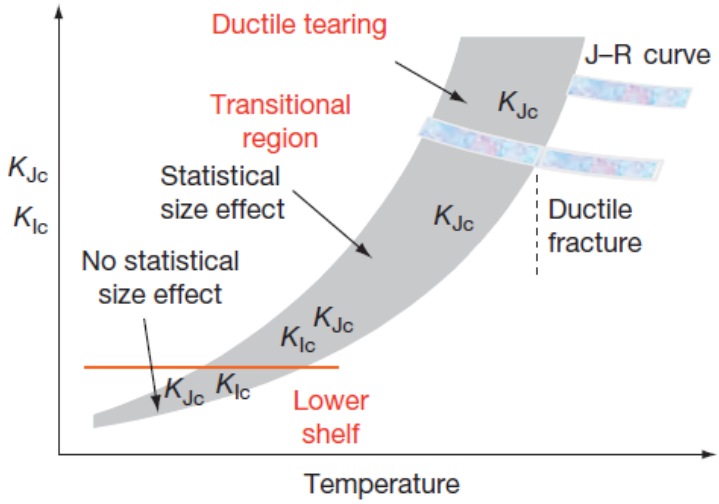

Figure 6 Graphic description of the fracture toughness transition region including value parameters used to characterise fracture toughness.
(Planman and Server, 2012)

Plastic deformation requires a mechanism of dislocation multiplication. At low temperatures thermal enhancement of dislocation motion is limited and, thus, the bcc ferrite microstructure is incapable to deform plastically due to the inability of screw dislocations to cross slip, Figure 7. Consequently, screw dislocations are bound to separate slip planes and cannot participate to a mechanism of dislocation multiplication. Near the upper shelf at increasing temperatures, the cross-slip mechanism of the screw dislocations is possible as presented in Figure 8. Hence, active slip systems allow more plastic deformation that precedes ductile tearing and fracture. Moreover, metals with bcc crystal structure contain narrow dislocations. (Grauss, 2015; Hertzberg et al., 2013)

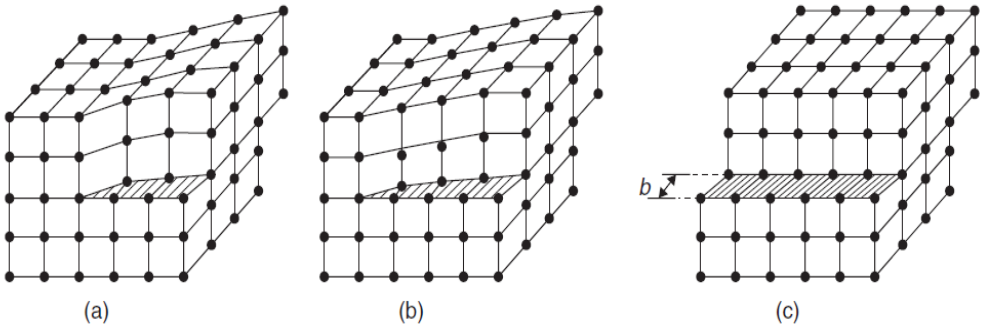

Figure 7 A screw dislocation causes a slip.
(Smallman and Ngan, 2007)

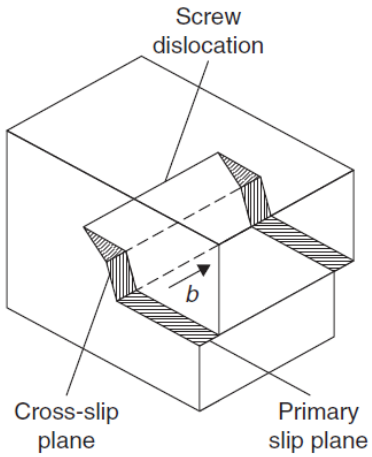

Figure 8 A cross-slip of a screw dislocation.
(Smallman and Ngan, 2007)

In the ductile-to-brittle transition region both ductile and cleavage fracture may occur. At low temperatures close to the lower shelf, the fracture mode is cleavage and a brittle surface has a flat, grainy and shiny surface texture. In the upper transition region close to the upper shelf, the mechanism of the fracture changes to ductile and cracks initiate by micro-void coalescence. The fracture surface appears dim and rough. Due to the variation of fracture modes in the transition region, fracture toughness data tend to be remarkably scattered. (Anderson, 2005; Callister, 2007)

2.2 Nature of ductile crack growth

Prior to fracture, ductile material has the capability to deform plastically permanently. Qualification of ductility and toughness are related; both have aforesaid capability and moreover the ability to absorb energy. A characteristic to ductile fracture is that, before any other mode of fracture may occur, shear stress must exceed shear strength. Specific to ductile crack propagation is that it stops when deformation stops. (Campbell, 2012)

A common mechanism of ductile crack nucleation is the void forming around inclusion or second-phase particle, Figure 9. At adequate stress level, the particles debond at the interface and void nucleation begins (see Figure 10.1). As a consequence of applied stress, nucleated voids continue to grow (see Figure 10.2) and eventually coalesce (see Figure 10.3) resulting in failure.

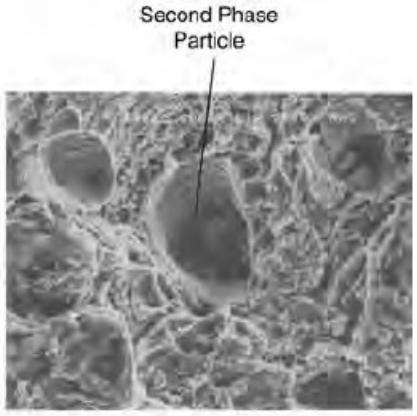

Figure 9 A second-phase particle in a ductile material.
(Campbell, 2012)

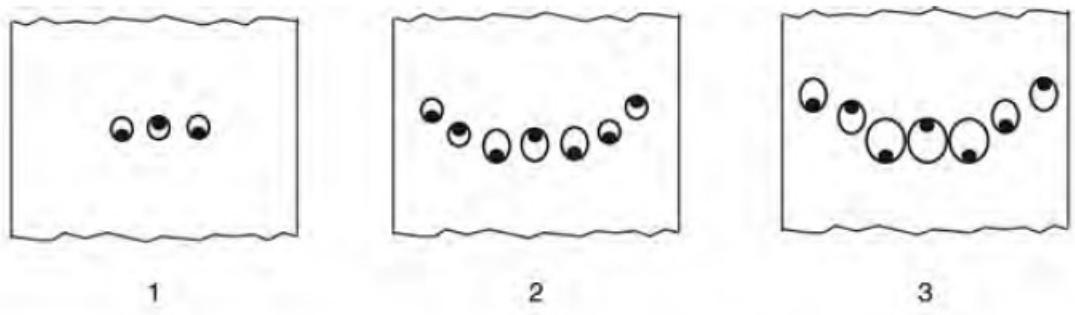

Figure 10 Nucleation, growth and coalescence of microvoids in ductile cracking.
(Campbell, 2012)

The growth and coalescence of voids are considered to be the crucial step in ductile crack growth. As the voids grow, between them develops a local plastic instability which conveys to coalescence of microvoids. Ductile crack growth, however, is usually steady. (Anderson, 2005; Campbell, 2012)

2.3 Nature of brittle crack growth

Unlike ductile fracture, brittle fracture is sudden and precedes none at all or an insignificant amount of plastic deformation. Brittle fracture, also known as cleavage fracture, may lead to catastrophic failure due to its nature. Once cleavage crack has initiated, propagation occurs rapidly throughout the material. Several factors do influence to the initiation of cleavage fracture; such as low temperature, grain size or whether nucleation occurs at twins or at carbides (Krauss, 2015). Particularly, the grain size is a substantial matter in ferritic steels involving cleavage fracture and hence transition temperature. This stems from the fact, that cleavage fracture toughness decreases steeper than yield strength when the grain size increases. (Miekkoja, 1965)

2.3.1 Nucleation of cleavage crack

Bcc steels are polycrystalline; each grain is surrounded by other grains. Cleavage fracture favours planes with low packing density by reason of accessible propagation. In such planes, the lattice distance is larger and fewer bonds occur to be broken. Favourable {100} planes, three possible, are represented in Figure 11. (Anderson, 2005; Stec and Faleskog, 2009)

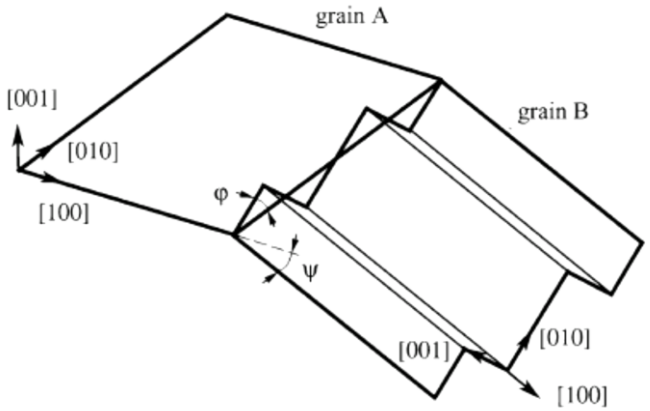

Figure 11 Characteristic presentation of cleavage planes of adjacent grains A and B. (Stec and Faleskog, 2009)

As seen in Figure 11, the orientation of the planes differs between adjacent grains, hence grains generally attach only at specific points. This kind of misorientation can be described with a tilt angle ψ and a twist angle φ.

In common, crack nucleates when the local strength of the material is exceeded by the local stress. Cleavage crack tends to form inside a grain (see Figure 12a, top view); initiation requires a local discontinuity (such as an inclusion) before the microscopic crack nucleates. Moreover, the discontinuity needs to be adequate enough to surpass the bond strength. If not, crack propagation is arrested and total fracture does not occur. Crack propagation may arrest as well if an abrupt stress gradient lies ahead of the macroscopic crack. (Anderson, 2005; Stec and Faleskog, 2009)

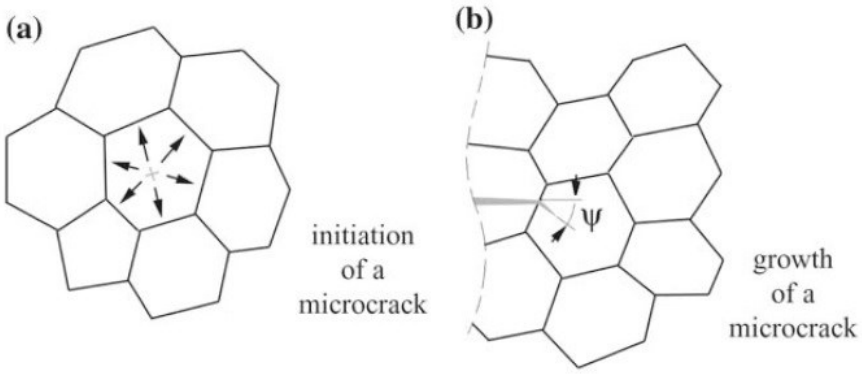

Figure 12 Initiation a) and growth b) of a microcrack.
(Stec and Faleskog, 2009)

In Figure 13 is represented the mechanism of cleavage initiation in ferritic steels. The stress and strain are concentrated locally in the crack tip. The surrounding matrix suffers from plastic strain and thereby second-phase particle cracks. The microcrack continues propagating into the ferrite matrix solely, if adequate stress precedes the macroscopic crack. The consistency of the second-phase particle depends on the alloy and thermal treatment. In quenched and tempered steels, such as discussed in this thesis, the second-phase particle is commonly either an inclusion or spherical carbide. (Anderson, 2005)

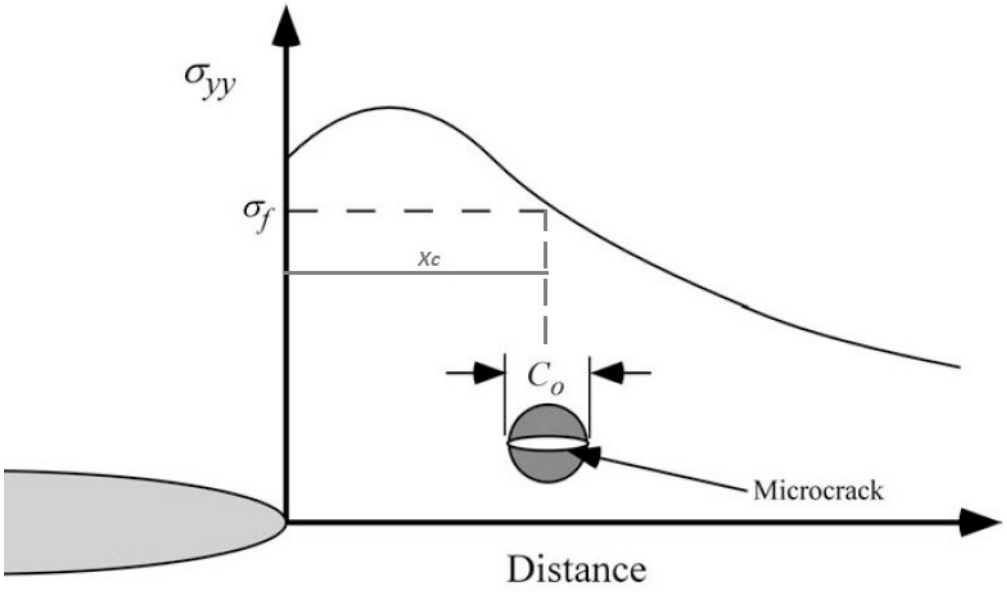

Figure 13 The mechanism of cleavage initiation in ferritic steels.
(Modified)
(Anderson, 2005)

In Figure 13 σ_{yy} is a plane stress and σ_f is a failure stress; C_0 describes size of initiated microcrack and X_c is the characteristic distance.

2.3.2 Crack propagation

Conversely to stable nature of ductile cracking process, brittle cracking process is more unstable and has been referred even crucial by the fact that propagation may rapidly lead to final fracture. In cleavage fracture the crack may propagate with a sound velocity and crack with a loud noise (Liu, 2005). Nucleation of the crack requires a crucial value of the effective shear stress to be reached, whereas propagation depends on the extent of the local tensile stress which must reach a crucial level σ_f. (Bhadeshia and Honeycombe, 2006)

In Figure 12b (side view) is a view how after initiation crack propagates towards the grain boundaries. Each time when a consecutive grain is encountered, the propagating crack changes direction. Characteristic to cleavage crack propagation is that crack chooses the most favourable planes (Figure 11) in each grain. It may be tilted or twisted orientation and it diverges from grain to grain (Anderson, 2005; Stec and Faleskog, 2009). Another common feature is when propagating from grain to grain, the crack will propagate through the entire cross-section (Engel and Klingele, 1981). In Figures 14 – 17, is represented cleavage fracture, first in sketch followed by actual photo, crossing a tilted grain boundary and subsequently crossing a twisted grain boundary.

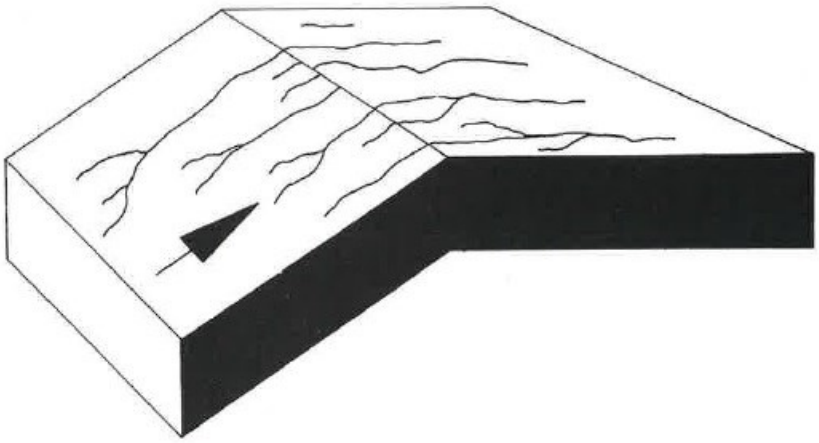

Figure 14 Cleavage cracking crossing a tilted grain boundary.
(Engel and Klingele, 1981)

When crossing a grain boundary, cleavage fracture tends to branch into several, parallel cracks in consequence of the orientation difference between the grains. Consequently, cracks are able to unite as propagation resumes and orientation continues to differ. The arrow in Figure 14 indicates the direction of the crack origin (Engel and Klingele, 1981).

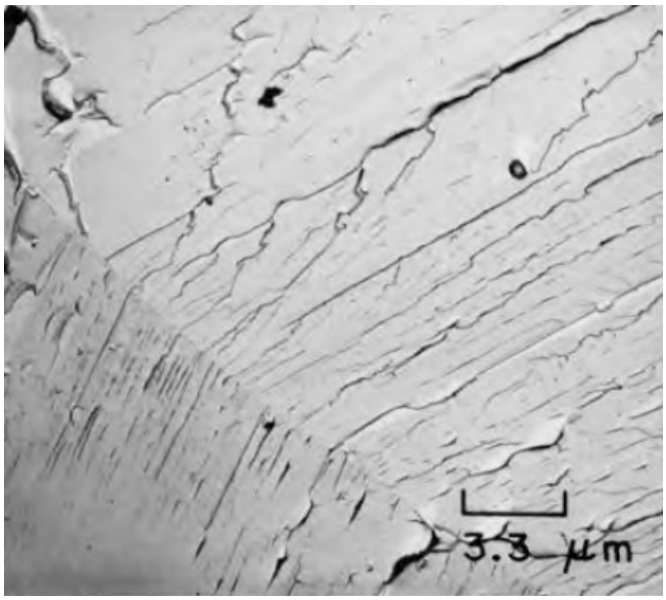

Figure 15 TEM photo of cleavage cracking crossing a tilted grain boundary. (Campbell, 2012)

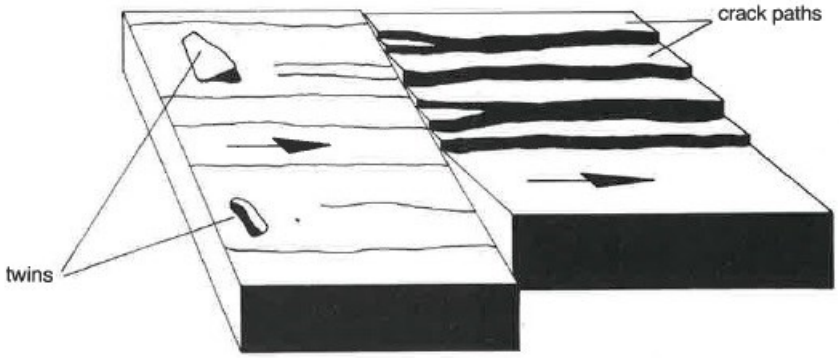

Figure 16 Cleavage cracking crossing a twisted grain boundary. (Engel and Klingele, 1981)

In bcc metals, due to the decrease of temperature and the rapid increase of the flow stress of iron, twinning, together with prior slip, is often seen as a remarkable deformation mechanism. Twins (see Figure 16) are formed at the tip of the propagating crack such that crack leaves from the favourable {100} plane and transfers to proceed alongside the twin {112} boundary. The points where twins contact grain boundary, and twin intersections, are shown to be points where cracks will preferentially initiate at various twin orientations. After the crack branching at the twin, the crack subsequently reverts to a primary {100} plane. (Bhadeshia and Honeycombe, 2006; Engel and Klingele, 1981)

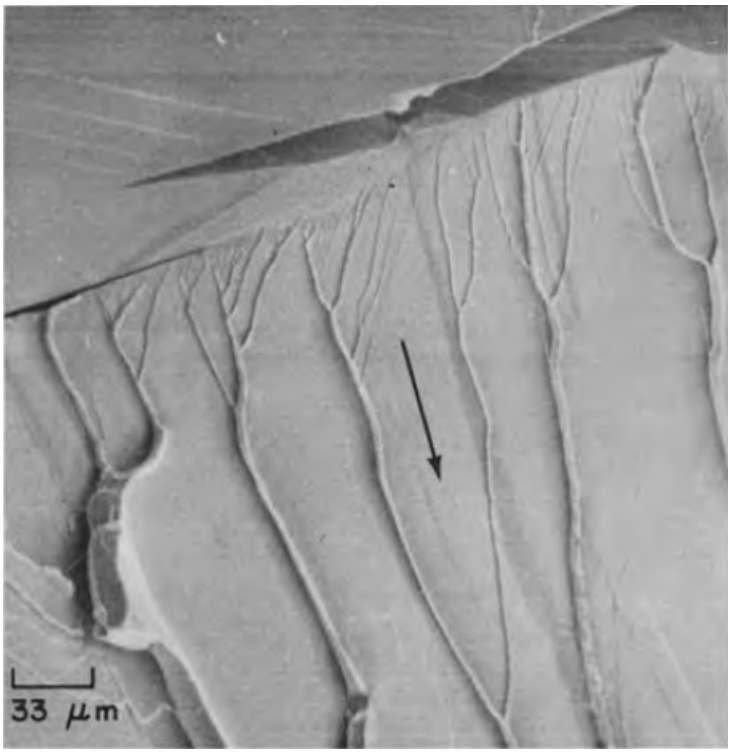

Figure 17 SEM photo of cleavage fracture crossing a twisted grain boundary. (Campbell, 2012)

Herringbone patterns, shown in Figure 17, are composed of a series of crack initiations. Such patterns are extraordinary microscopic properties of cleavage fractures. The cleavage on a {100} plane forms the central spine of a herringbone when branching of the crack occurs at twinning planes {112}. Besides of herringbone patterns, brittle fracture mechanisms may display chevron patterns as an indication of the fracture origin, as well as the direction of fast fracture propagation. (Liu, 2005)

In preceding figures arrows indicate the location of crack origin; direction of propagating is deduced from crack branching. Furthermore, the direction of crack propagation should correspond to the internal state of stress caused by the external loads. (Liu, 2005)

2.3.3 Maximum stress

As mentioned, in order for cleavage fracture to evolve, the local stress must be sufficient enough to break bonds and consequently exceed the cohesive strength of the material. Moreover, propagation direction needs to correspond to the internal state of stress. Hence, the nominal direction of the cleavage crack is vertical to the maximum stress which is three to four times the material yield strength. The maximum stress precedes the crack and appears at approximately two times crack-tip-opening displacement, 2δ, from the crack tip, see Figure 13 for more clarification. The distance is variable and changes with increasing or decreasing K, J and δ. (Anderson, 2005)

In Figure 18 is shown a relation between fracture toughness J_c, the critical distance r_c and the location of the maximum stress. As seen, cleavage nucleates near the location of the maximum stress. In such context, the critical distance stands for the distance from fatigue pre-crack tip to the cleavage nucleation site (Anderson, 2005). Wallin, Yamamoto and Ehrnstén (Wallin et al., 2016) have also examined the location of cleavage initiation sites focusing on the miniature C(T) specimen.

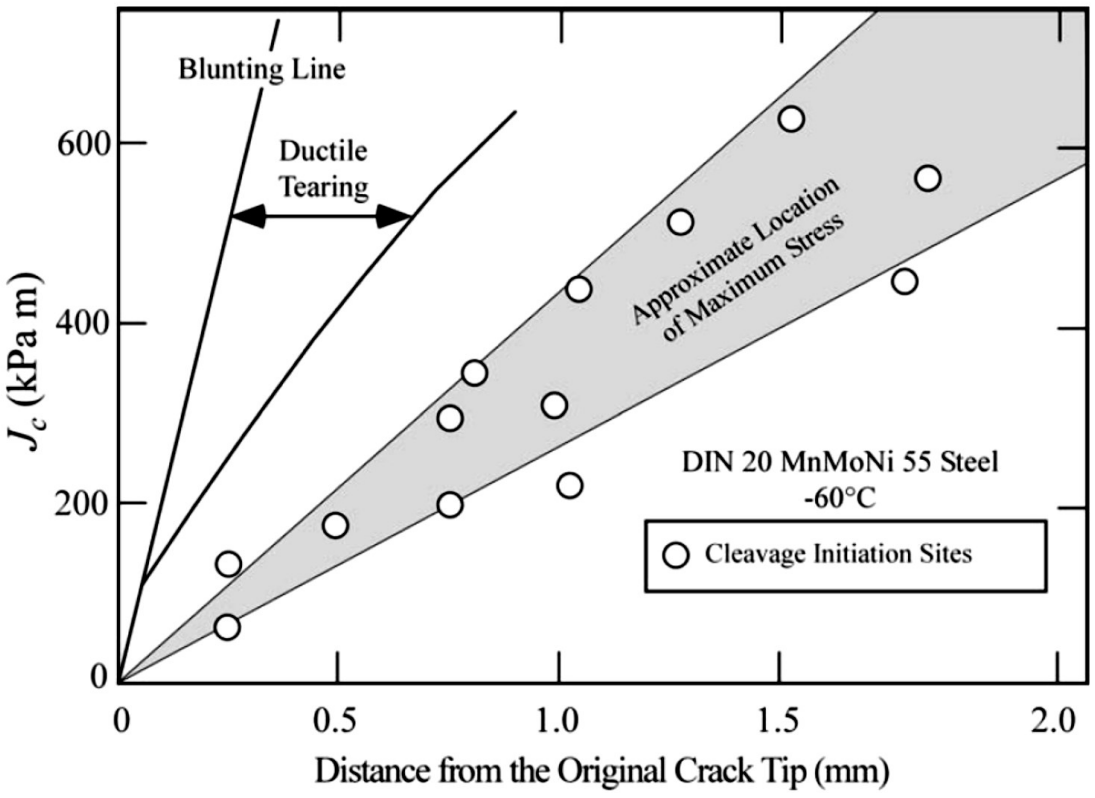

Figure 18 Fracture toughness vs. critical distance showing of approximate location of maximum stress. (Anderson, 2005)

A scientific assumption has been made related to above-mentioned critical distance, one of them by Ritchie, Knott and Rice. According to them, cleavage failure is assumed to appear when the stress preceding crack tip surpasses the critical fracture stress σ_f over a

characteristic distance X_c. This phenomenon is illustrated in chapter 2.3.1 in Figure 13. (Ritchie et al., 1973)

2.3.4 Statistical effect

A statistical ground for a critical distance has been presented as well; Curry and Knott stated that a limited amount of material needs to be sampled in front of the crack tip. Intention is to determine a particle, a fracture-triggering particle, capable enough to initiate cleavage fracture. Added to that, the plane stress σ_{YY} must equal or exceed the critical fracture stress σ_f in order to breakdown. The average distance of cleavage initiation sites determines the critical volume of samples needed. Since the area of the crucial fracture-triggering particle tends to be occasional, thus cleavage fracture toughness data is broadly scattered and fracture toughness values may extensively differ even within specimens manufactured from the same material. (Curry and Knott, 1979)

The statistical character of cleavage fracture additionally has an influence for a thickness effect on toughness. Thicker the specimen, larger the fracture-triggering particle and lower the toughness value. Subsequently, the approach by Curry and Knott was followed by further models for cleavage fracture phenomena. Models were based on a weakest link theory, where the probability of sampling at least one crucial fracture-triggering particle and the probability of fault equals. The probability of failure can be concluded from the Poisson distribution in Eq. 1:

$$F = 1 - exp(\rho V) \tag{1}$$

where:

F	is probability of failure
ρ	is amount of critical particles per unit volume
V	is volume of material

Moreover, the Master Curve theory is based on the weakest link theory.

2.3.5 Irradiation embrittlement

An increase in ductile-brittle transition temperature is a common way to characterize irradiation embrittlement; as much as 200 - 250°C increase is being possible. During service, ferritic RPV steels suffer from microstructural alterations, which primarily stem from hardening of steel. As a consequence of radiation, high-energy neutrons, which are dominating in embrittlement, cause nanometer-size features and hardening. (Odette and Lucas, 2001)

Such microstructural alterations are induced by mutual reaction of neutrons and metal atoms. Crystal lattice consists of metal atoms with a certain location; however, neutrons are able to knock atoms from their original sites. Consequently, migrated atoms become interstitial atoms leaving at the original location a vacancy. A displaced atom is also capable of knocking out other atoms from their lattice site, in case of primary neutron impact being adequate enough. Neutron radiation generates such circumstances in which

the multiplication of dislocations (previously in chapter 2.1) becomes challenging and thus, the ductility is reduced. (Engel and Klingele, 1981; English and Hyde, 2012)

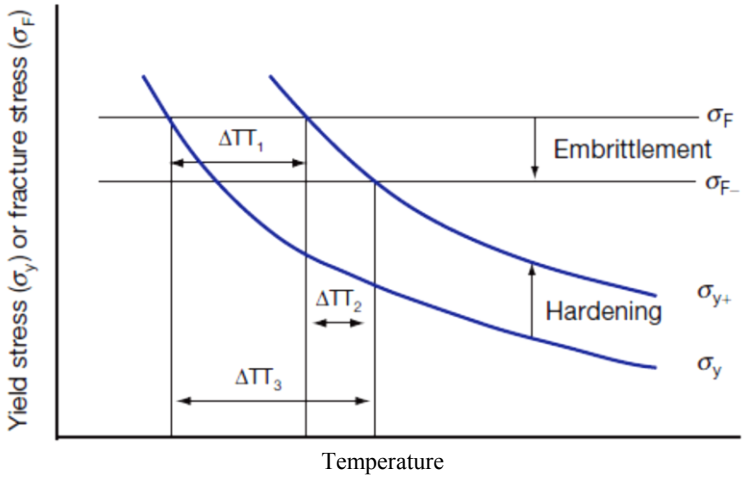

Figure 19 Dependency of yield stress and fracture stress on temperature. (English and Hyde, 2012)

In Figure 19 is clarified the influence of embrittlement and hardening through variation of yield stress σ_{YS} and fracture stress σ_f on temperature. At present moment the effect of radiation damage on ferritic RPV steels has been considered in terms of i) the development of matrix damage; crystal lattice defects, ii) the radiation emphasized development of copper enriched clusters and iii) the grain boundary segregation of embrittling species such as phosphorus. The mechanisms i and ii increase the yield strength, whereas decrease of fracture strength is affected by the mechanism iii. As Figure 19 shows, the yield strength and the fracture strength are temperature dependent; an increase in σ_{YS} induces DTT1, while irradiation-enhanced grain boundary segregation may reduce σ_f resulting in an alteration of DTT2. A compounded alteration of DTT3 exists when both mechanisms are in function. (English and Hyde, 2012)

2.4 Master Curve theory

The Master Curve methodology is based on a cleavage fracture model and it includes two key features: a statistical model of the cleavage fracture and a temperature dependency of fracture toughness common for all ferritic steels; moreover, it is presumed that the material consists randomly distributed defects or cleavage fracture initiators. The cleavage toughness data tends to be extremely scattered, as interpreted in chapter 2.3.4, particularly in the transition range. Hence, Master Curve methodology works best in the ductile-brittle transition region, see Figure 7. (IAEA-TECDOC-1631, 2009; McCabe et al., 2005)

The formula Eq. 2 describes the temperature dependence of a median toughness in the ductile-brittle transition region. Though the MC model covers practically all ferritic steels, the procedure in ASTM E1921 'Standard Test Method for Determination of Reference Temperature, T_0, for Ferritic Steels in the Transition Range' is identified for ferritic steels with yield strength between 270 and 870 MPa.

$$K_{Jc(med)} = 30 + 70\, exp[0.019(T - T_0)] \tag{2}$$

where:

$K_{Jc(med)}$	is median fracture toughness [MPa√m]
T_0	is reference temperature [°C]
T	is test temperature [°C]

When $T = T_0$, median fracture toughness is 100 MPa√m, Figure 20, and it is a reason of the E1921 testing (ASTM E1921, 2015). In Figure 20 F is the probability of failure.

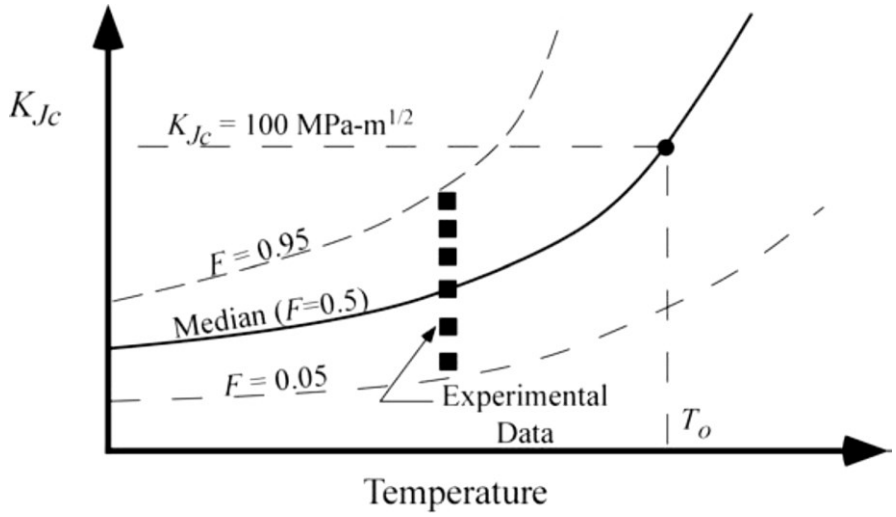

Figure 20 The fracture toughness Master Curve. (Anderson, 2005)

2.5 Fracture mechanics concept

The two very common fracture mechanics concepts are linear elastic and elastic-plastic. There are two parts that separates them; stability of a state and a response after being loaded. Linear-elastic materials are reversible; they do not achieve steady deformation contrary to elastic-plastic materials. Elastic-plastic and linear-elastic materials behave the same way when loaded, but recovery diverges. This behaviour is described in Figure 21.

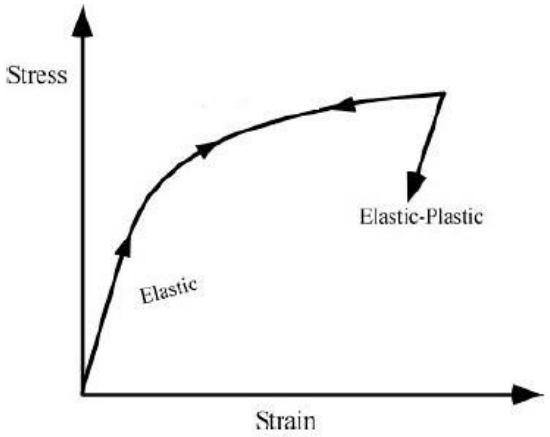

Figure 21 Stress-strain behaviour of elastic and elastic-plastic materials. (Modified) (Anderson, 2005)

It is practically impossible to describe with linear-elastic fracture mechanics (LEFM) the fracture behaviour, since it is valid only for a small area surrounding the crack tip. Contrary to LEFM, elastic-plastic fracture mechanics is applied to materials with two parameters that describe crack-tip conditions. These parameters are crack-tip-opening displacement (CTOD) and the *J* contour integral. (Anderson, 2005)

2.6 Methodology of ASTM E1820

Fracture toughness describes how well material resists fracture, when a crack is present. High fracture toughness values lead to ductile material behavior and low fracture toughness values to more brittle material behavior. Fracture toughness, K_C, can be expressed as a combination of crack length (a) and critical stress for crack propagation (σ_C):

$$K_c = Y \times \sigma_C \sqrt{\pi a} \tag{3}$$

where:

K_C	is fracture toughness [MPa√m]
Y	is constant related to specimens geometry
σ_c	is critical stress for crack propagation [MPa]
a	is crack length [mm]

In Eq. 3, Y is a unitless parameter that depends on the size of a crack and a specimen, also the specimen geometry affects. In addition, mode (opening, sliding or tearing) of load application influences to Y. The specific unit of K_C is crucial to notice, MPa√m. (Callister, 2007)

Fracture toughness values may be utilized for materials comparison, materials selection or quality assurance. Moreover, it can be used to rank materials within a similar yield strength range or serve as a basis for structural flaw tolerance assessment. (Callister, 2007)

2.6.1 Test specimens

ASTM E1820 is based on the usage of standardized test specimens and in Figure 22 are two most commonly used test specimens; a compact-tension specimen (C(T)) and a single-edge-notch bend specimen (SE(B)). Load modes are described according to tension type for the C(T)-specimen and bending for the SE(B) specimen.

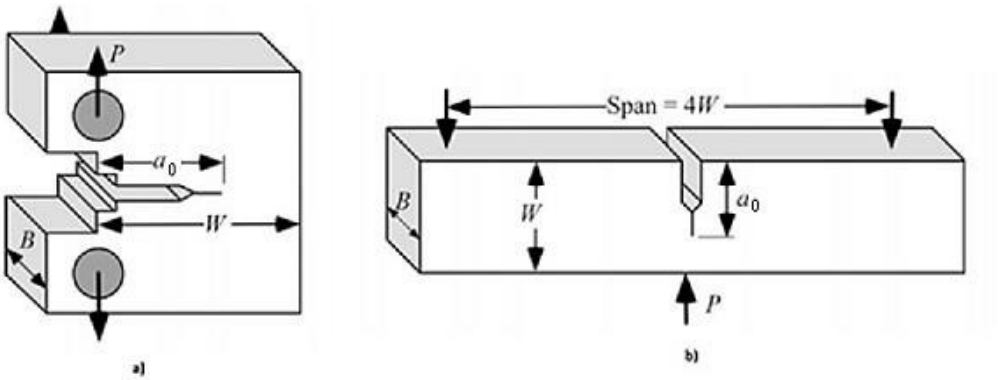

Figure 22 Two common fracture toughness test specimens: a) C(T)-specimen, b) SE(B)-specimen. (Modified)
(Anderson, 2005)

Dimensions are: W = width (mm), B = thickness (mm), a_0 = pre-cracked (initial crack) length (mm). P denotes a direction of the loading and in Figure 22b; $4W$ is a span for supporting rolls. Often $W = 2B$ and the crack aspect ratio $a/W = 0.5$, though there appears variation. (Anderson, 2005)

2.6.2 Test method

The objective of this test method is to pose either fracture instability (unstable crack extension) or stable tearing (stable crack extension) and that is accomplished with compliance process. In fracture toughness method both force versus load-line displacement and crack-mouth-opening displacement are under continual measurement. Measured values are presented in Figures 23 and 24. Test procedure continues until either the operator interrupts the test or a set limit is achieved. Possible set limits are, e.g., a range of the crack-opening displacement (COD) gage or a displacement of the clevis (ASTM E1820, 2015). More detailed description of the experimental arrangements is presented in chapter 4.

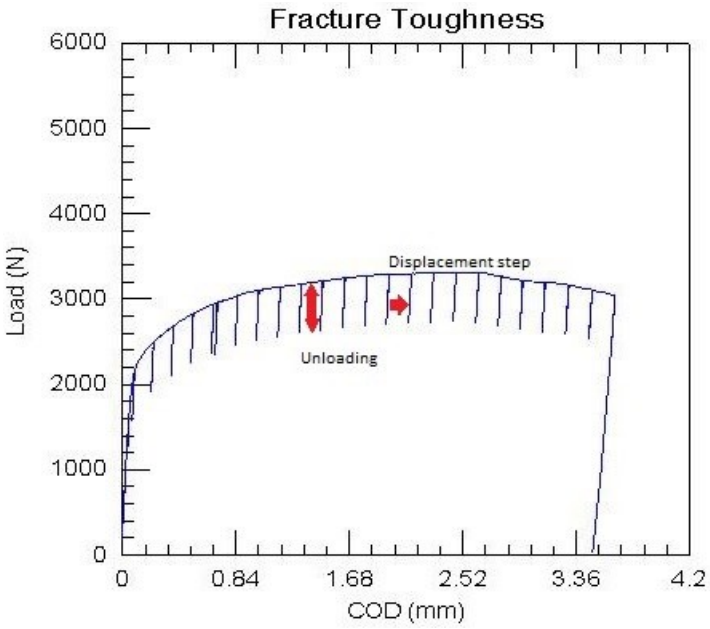

Figure 23 Load versus crack-opening displacement.

The displacement step is executed under COD control and the load-unload step under force control. The intention is to accomplish a controlled test, but of course an unstable crack growth is beyond control. The resistance curve procedure is an elastic compliance method where multiple points are determined from a single specimen. The procedure aims to have a required amount of controlled compliances (points) between exclusion lines, Figure 24. Thus qualifications of ASTM E1820 standard are fulfilled and determination of fracture toughness is possible.

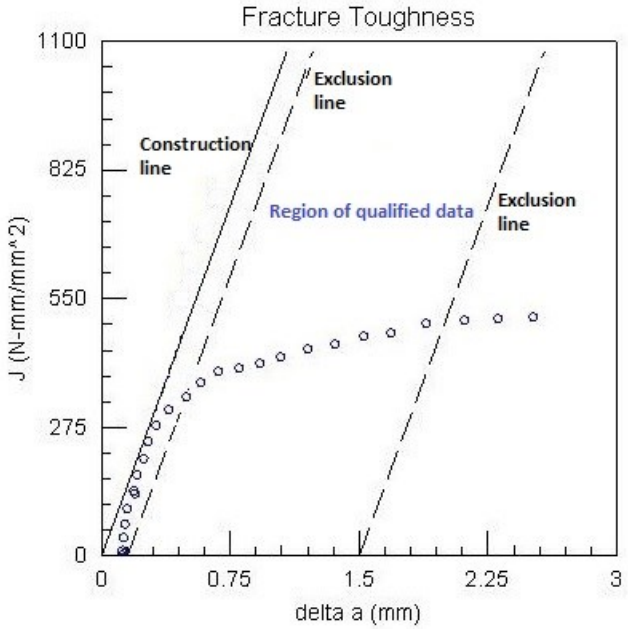

Figure 24 J-R curve of the test method ASTM E1820.

J (MJ/m^2), in ordinate, is used to characterize the local stress-strain field around the crack front and the Δa (m) is the crack extension. Overall, the material fracture resistance curve,

J-R curve, represents the crack extension resistance as a function of a stable crack extension.

In the beginning of chapter 2.6 a simplified meaning for fracture toughness was mentioned; it describes materials resistance to fracture when a crack is present. Having a look to more detailed level, the material fracture toughness values by this test method are divided in four different categories. These values characterize materials resistance to: (a) fracture of a stationary crack, (b) fracture after some stable tearing, (c) stable tearing onset, and (d) sustained stable tearing. (Anderson, 2005)

2.6.3 Analyses

The J-integral, presented in chapter 2.5, is divided into two parts; plastic J_p and elastic J_e:

$$J = J_p + J_e \tag{4}$$

where:

J	is J-integral
J_p	is plastic component of J [MJ/m^2]
J_e	is elastic component of J [MJ/m^2]

Eq. 4 is valid for both CT-specimen and SE(B); J is distinguished for elastic and plastic components. However, calculations for fracture toughness are different depending on the test specimen. Eq. 5 indicates formula for three-point bending specimen and Eq. 6 for compact-tension specimen (ASTM E1820, 2015). *f(a/W)* is a dimensionless function that reflects the geometry and mode of loading of the specimen. (For *f(a/W)* further clarifications are given in standard ASTM E1820.)

$$K = \left[\frac{PS}{(BB_N)^{1/2}W^{3/2}}\right] f\left(a/W\right) \tag{5}$$

$$K = \left[\frac{P}{(BB_N W)^{1/2}}\right] f\left(a/W\right) \tag{6}$$

where:

K	is fracture toughness [MPa√m]
P	is load [N]
S	is span for supporting rollers [mm]
B	is specimen thickness [mm]
B_N	is specimen net thickness [mm]

W	is specimen width [mm]
$f(a/W)$	is dimensionless function that reflects the geometry and mode of loading of the specimen

Furthermore, the crack-tip-opening displacement (CTOD) can be calculated from any point of the force-displacement curve. The following expression, Eq. 7, requires material yield strength divided by ultimate tensile strength to be 0.5 or more (ASTM E1820, 2015). (The equation for *(m)* is given in ASTM E1820.)

$$\delta = \frac{J}{m\,\sigma_Y} \tag{7}$$

where:

δ	is crack-tip-opening displacement [mm]
J	is J-integral
m	is constraint factor
σ_{YS}	is yield strength [MPa]

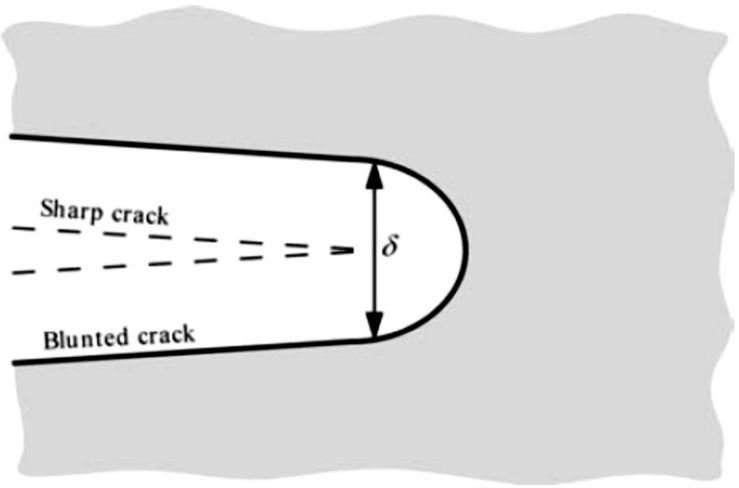

Figure 25 Crack-tip-opening displacement (CTOD). (Anderson, 2005)

Figure 25 demonstrates a phenomenon, where plastic deformation causes an initially sharp crack to blunt, and as a result a finite displacement (δ) occurs at the crack tip.

During the test, there always appears slight rotation in the test specimen. Consequently, to diminish the influence of the rotation a crack growth needs to be corrected computationally. In addition, crack size values are obtained with an optical microscope from the post-test fracture surface, since crack lengths generally vary through the thickness of the test specimen (Anderson, 2005).

Based on optical measurements, a nine-point average procedure is used to receive a reportable crack size (ASTM E1820, 2015). This procedure is shown in Figure 26; a post-tested specimen, with a ductile fracture, which has been in the furnace at 300 °C for approx. 30 min.

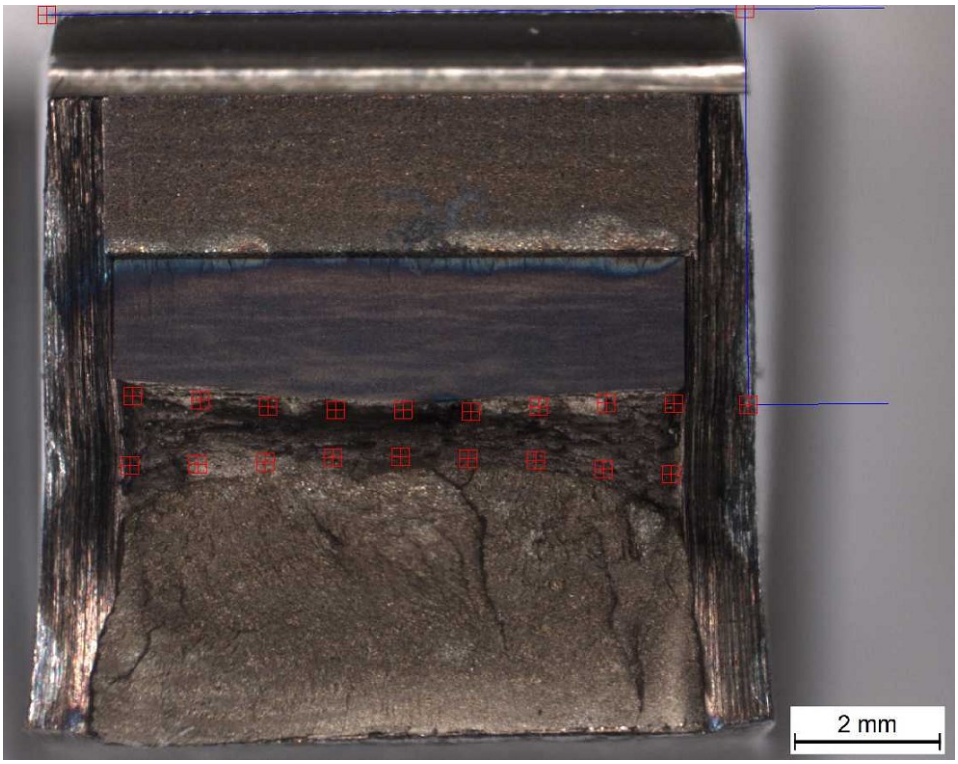

Figure 26 A nine-point average procedure to measure the crack length.

2.7 RPV materials and manufacturing

Most RPVs are manufactured from pressure vessel steel type SA 508 Class 2 or Class 3 ring forgings which possess high toughness in the unirradiated state (May et al., 2015). High fracture toughness in large forgings requires fine grain size together with a proper microstructure and a shift of the transition temperature curve, in Figure 3, is influenced specifically by the contents of copper and phosphorus. Consequently, levels of copper and phosphorus are restricted particularly in the belt line region forgings. Moreover by manufacturing RPVs from forgings instead of steel plates weld seams can be avoided in the belt line region (Ando, 1980). Such structure compared to plate design is presented in Figure 27.

On the other hand, in the quenched and tempered low-alloy steels the use of nickel alloying specifically lowers the ductile-brittle transition temperature and at the same time increases the toughness. (Kou, 2003)

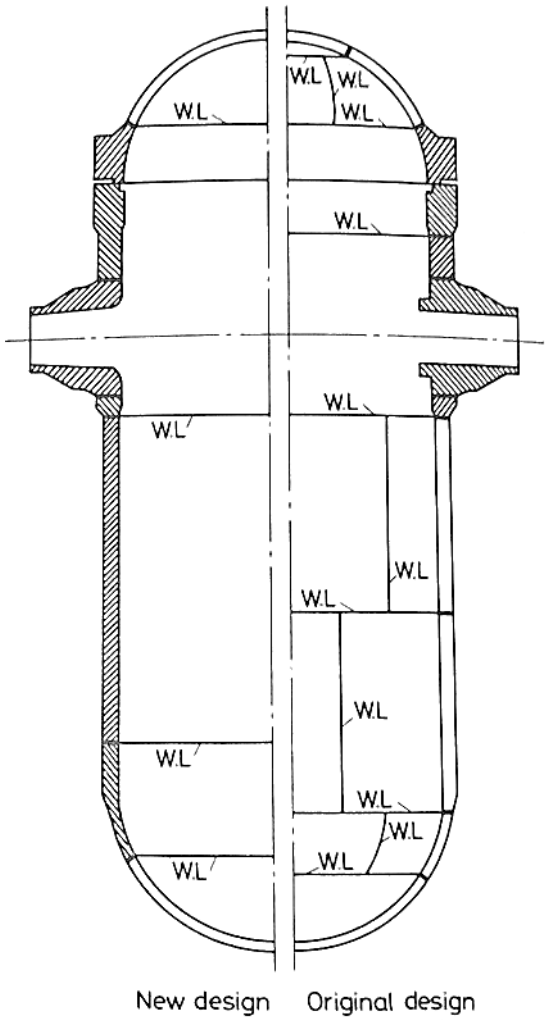

Figure 27 The original steel plate design compared to the new forging design of RPV. (Ando, 1980)

From Figure 27 can be seen the difference in the amount of weld seams; from eleven down to four seams with no weld seams at the belt line region.

2.7.1 Welding

Majority of welded pressure vessels are manufactured by using arc welding procedure; for low-alloy steel vessels the most commons are the submerged arc, the manual metal arc and the electroslag processes (Rogerson, 1980). Preceding processes belong to the consumable electrode welding arc category, in which the electrode is melted and the molten metal is carried across the arc rift. In the arc welding process the heat cycle is of primary concern; the changes of temperature are intense due to the fact, that the metal reaches a superheated temperature exceeding the melting point. Consequently, the molten metal transmits the heat into the base metal by raising its temperature on the same level. The melted base metal mixes up with the weld metal producing a dilution of weld metal. At the final stage of the heat cycle the liquid weld metal freezes and crystals form into grains. (Cary and Helzer, 2005)

In addition, the thermal cycle causes segregation that relates to the solubility of alloying elements such as carbon, phosphorus and sulphur. Melting points of the elements differ and hence, the composition varies due to the solidification time and may cause lack of homogeneity in weld metal. However, particularly segregation of carbon can be influenced by heat treatment. (Cary and Helzer, 2005)

2.7.2 Residual stresses

Residual stresses caused by welding, often called thermal stresses, stem from temperature changes; stresses occur either in tensile or compressive form. Residual tensile stresses tend to occur in weld metal adjacent to the base metal, whereas areas farther away from the weld seam suffer from residual compressive stresses, see Figure 28. (Kou, 2003)

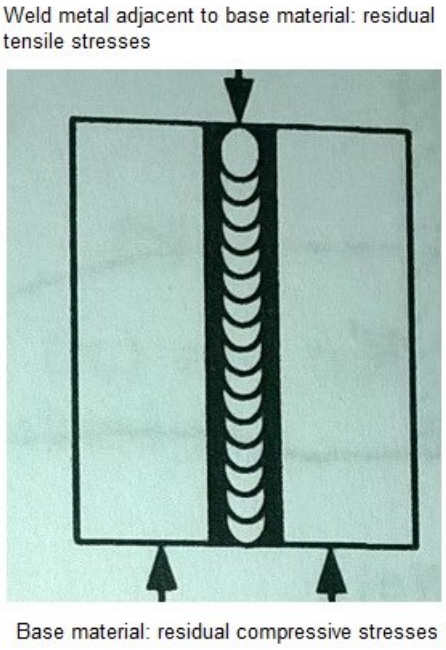

Figure 28 Residual stresses in and around weld.
(Modified)
(Kou, 2003)

However, as has been observed, thick-walled structures contain tensile residual stresses in preference to compressive stresses; these stresses may achieve even the level of weld metal yield stress (Sonsino, 2009). A post-weld heat treatment is one way of reducing residual stresses besides peening, which belongs to cold-working category.

2.7.3 Welding defects

Specifications and rules of safety for welding defects can be found in the Pressure Vessel Codes published by the American Society of Mechanical Engineers (ASME). Since the prevention of welding defects is practically infeasible or at least highly difficult, the Pressure Vessel Code specifies a tolerance level for minor defects. Notable matter as well is the remarkable costs of repair weld procedures and therefore the subject of weld defects is significant. (ASME, 2017; Rogerson, 1980)

An extensive classification of various types of weld defects is compiled by the International Institute of Welding (IIW), where defects are categorized into six main groups: cracks, cavities, solid inclusions, lack of fusion and penetration, imperfect shape and miscellaneous. The most of considerable defects are either cracks or lack of fusion and lack of penetration; low-alloy steels for nuclear vessels, such as SA 508, are found to be susceptible particularly for undercladding cracking, which resides into reheat cracking (Rogerson, 1980; Hamilton, 1980). An explanatory sketch of locations of reheat cracks is presented in Figure 29. Furthermore, a typical welding problem in low-alloy steels is occurrence of porosity which may be avoided by adding deoxidizers in filler metal. (Kou, 2003)

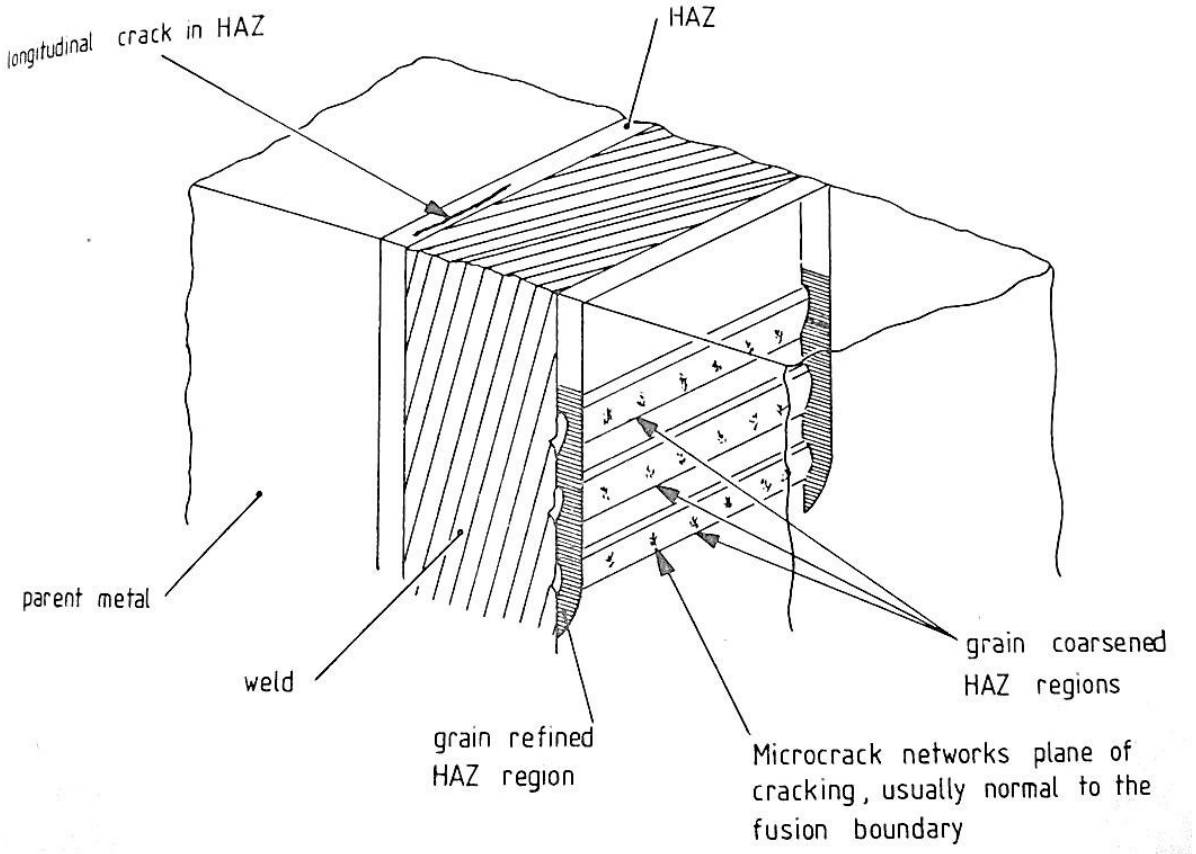

Figure 29 Reheat cracking sites in structural weld. (Hamilton, 1980)

In Figure 29, HAZ is the heat-affected zone; a region where the heat from welding diffuses causing changes in microstructure and mechanical properties of the material. There are two types of HAZ cracking; micro-cracks generally appear at grain-coarsened regions of HAZ perpendicular to the fusion boundary and macro-cracks passing through alternating microstructures length-wise to the welding direction. (Hamilton, 1980)

The majority of reheat cracks appears at the grain boundaries of the coarse-grained region of the HAZ, whereas typical hot cracking is a form of intergranular cracking which appears during or immediately after solidification, mainly in the weld metal. Yet another form of cracking which is combined with low-alloy ferrite steels HAZ is the cold cracking; typically transgranular appearing at low temperatures (< 150°C) and is evident some hours after welding (Rogerson, 1980). An image of heat-affected zone cracking is in Figure 30.

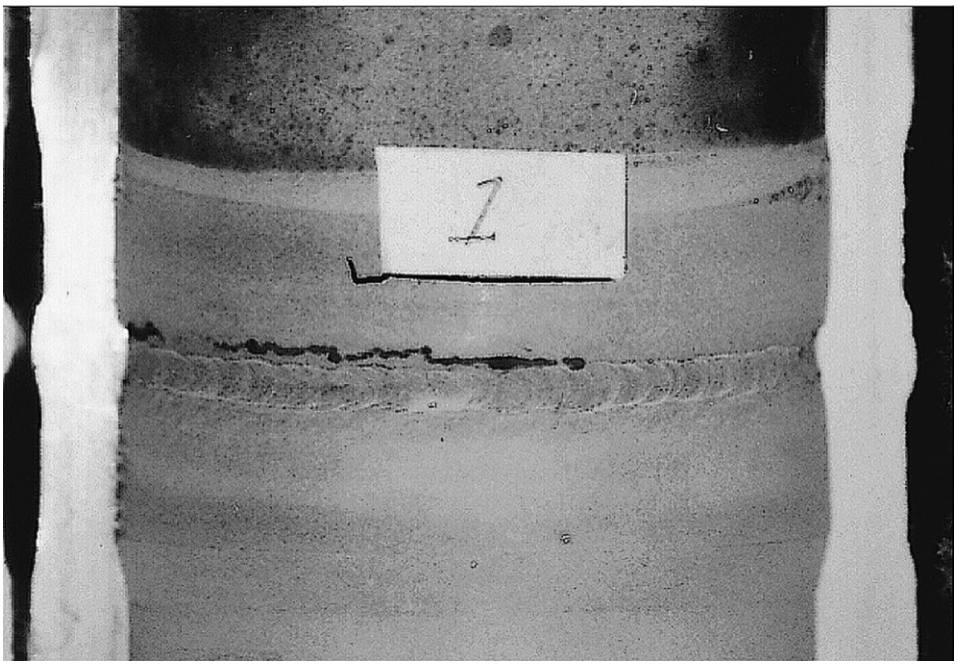

Figure 30 Cracking in the heat-affected zone of a pipe.
(Yamamoto et al., 2013)

2.7.4 Weld metal vs. base material

In Figure 31 is represented ferritic steel microstructures of three various regions nearby the weld; near fusion boundary, near base material from heat-affected zone and base material. Near the fusion boundary the ferrite form is acicular (Figure 31a), whereas farther away from the weld and its heat effect, in the base material, the grain size is less angular (Figure 31c). The acicular form of ferrite is desirable due to the fact that it improves the toughness of weld metal; acicular ferrite possesses the interlocking nature and together with its fine grain size it provides the maximum resistance to crack propagation by cleavage. (Kou, 2003)

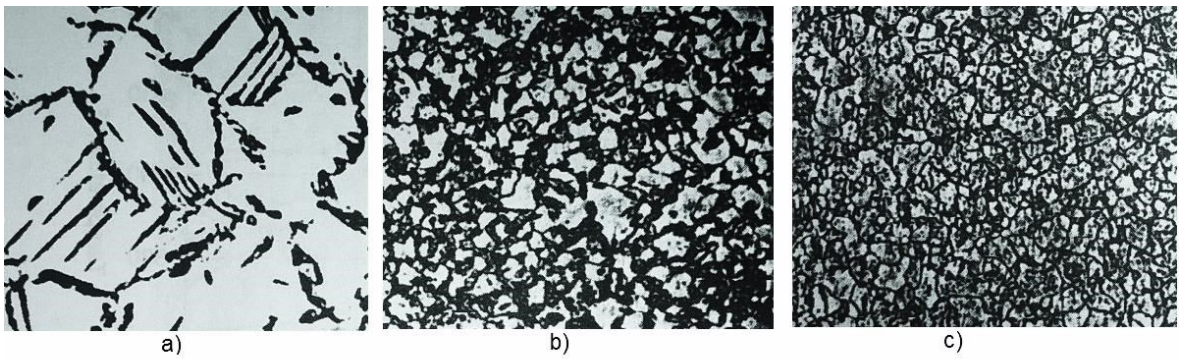

Figure 31 Microstructures (magnification 212x) of a) fusion zone, b) heat-affected zone and c) base material. (Kou, 2003)

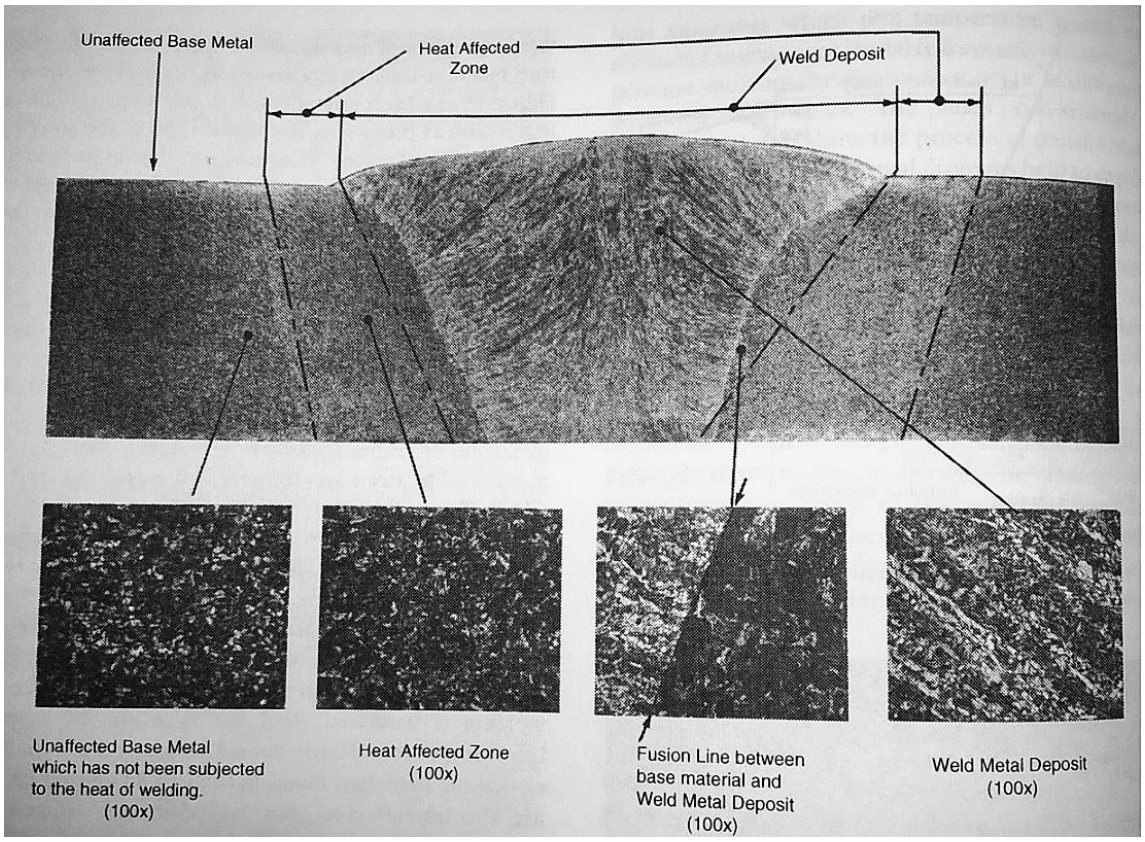

Figure 32 Different microstructures around weld. (Cary and Helzer, 2005)

The microstructure consists of phases present in the alloy, grain boundaries as well as comprehensive constitution of grains; each region around the weld has its own form of microstructure, such as in Figure 32. Both the grain size and the microstructure are related to strength and furthermore to hardness, which is one of the most essential characteristics of the microstructure around the weld area. The hardness is typically higher in the weld metal than in the base material and varies between these values in the heat-affected zone. (Cary and Helzer, 2005)

The heat-affected zone along with the admixture zone establishes a crucial area in many welds. In the hardenable base material, the heat-affected zone may increase the overall hardness to an undesirable level or alternatively become a softened zone. In the case of weld metal and base material having completely different analysis, the admixture zone consists of alloys that can be adverse, although commonly the properties of weld metal should match the properties of material being welded. (Cary and Helzer, 2005)

3 Materials and methods

An overview of test materials, Barsebäck 2 material and Ringhals 4 surrogate weld metal, studied in this thesis with manufacturing of test specimens, declaration of ASTM E1921 and metallographic characterisation are portrayed next.

3.1 Test materials

The test material consists of two different types of materials; the material B2 is a pressure vessel surveillance weld, HAZ and base material from the core region and represents the Barsebäck 2 NPP. The material R4 is a surrogate weld of a pressure vessel cover and comes from the Ringhals 4 NPP; both NPPs are located in Sweden. The Ringhals 4 NPP is a pressurized water reactor (PWR) that started commercial operation in 1983 and its intended decommissioning is in 2043, whereas the Barsebäck 2 NPP is a boiling water reactor (BWR), which has been decommissioned since 2005 after 28 years of commercial operation and consequently offers a unique opportunity to examine the RPV material (World Nuclear Association, 2017). The materials studied were in unirradiated state.

3.1.1 Chemical composition

The chemical compositions of Barsebäck 2 material and Ringhals 4 surrogate weld metal are presented in Tables 1 and 2.

Table 1. Chemical composition (wt. %) of Barsebäck 2 material. (Lydman et al., 2017)

	C	Si	Mn	P	S	Cr	Mo	Ni	Cu
Barsebäck WM	0.084	0.22	1.53	0.011	0.004	0.13	0.44	1.47	0.064

Table 2. Chemical composition (wt. %) of Ringhals 4 surrogate weld metal. (May et al., 2015)

	C	Si	Mn	P	S	Cr	Mo	Ni	Cu
Ringhals WM	0.068	0.14	1.35	0.015	0.004	0.04	0.50	1.66	0.05

3.2 Test matrix

The test matrix is given in Table 3. A total of 29 specimens were tested in order to determinate the transition temperature T_0 of Barsebäck 2 material and Ringhals 4 surrogate weld metal.

Table 3. Test matrix for determination of transition temperature T_0 of the weld metals studied.

B2 = as-welded weld seam of the RPV; specimens contain also HAZ and base material
R4 = surrogate weld seam of a top cap of the RPV
1 = notch direction parallel to CVN fracture surface
2 = no specified direction

Material	Notch direction	Specimen	Test Temperature °C
B2	1	BGK9.1	-120°C
B2	1	BGK9.2	-130°C
B2	1	BGK9.3	-130°C
B2	1	BGK9.4	-130°C
B2	1	BGN9.1	-100°C
B2	1	BGN9.2	-140°C
B2	1	BGN9.3	-140°C
B2	1	BGN9.4	-120°C
B2	1	BGK4.1	-130°C
B2	1	BGJ7.1	-140°C
B2	1	BGJ7.2	-130°C
B2	1	BGQ5.1	-140°C
B2	1	BGQ5.2	-140°C
R4	2	156 B	-100°C
R4	2	156 C	-100°C
R4	2	156 E	-100°C
R4	2	156 H	-100°C
R4	2	156 I	-100°C
R4	2	224.1	-130°C
R4	2	224.2	-130°C
R4	2	224.3	-130°C
R4	2	224.4	-120°C
R4	2	224.5	-120°C
R4	2	224.6	-80°C
R4	2	224.7	-120°C
R4	2	224.8	-110°C
R4	2	224.9	-90°C
R4	2	224.10	-100°C
R4	2	230 A	-100°C

3.3 Miniature C(T) specimen

Use of miniature size specimens, as a substitute for 'normal size' specimens, has become common in the nuclear power industry. Not only because of the volume of the material needed is less and for a possibility of re-use, but due to the fact, that ASTM E1921 allows the use of sub-size specimens to determine the fracture toughness in the ductile-brittle transition range. The latter feature is emphasized, since most of ASTM standards include size requirements. (Anderson and Dodds, 1993; Wallin et al., 2001)

3.3.1 Specimen dimensions

In Figure 33 is shown dimensions of the sub-size specimen; compared with a 'normal size' one inch specimen with a thickness of 25.4 mm, the sub-size specimen is under one sixth of it. The sizing is in accordance with ASTM E1820 and consequently such design is presented in Figure 34 for clarity.

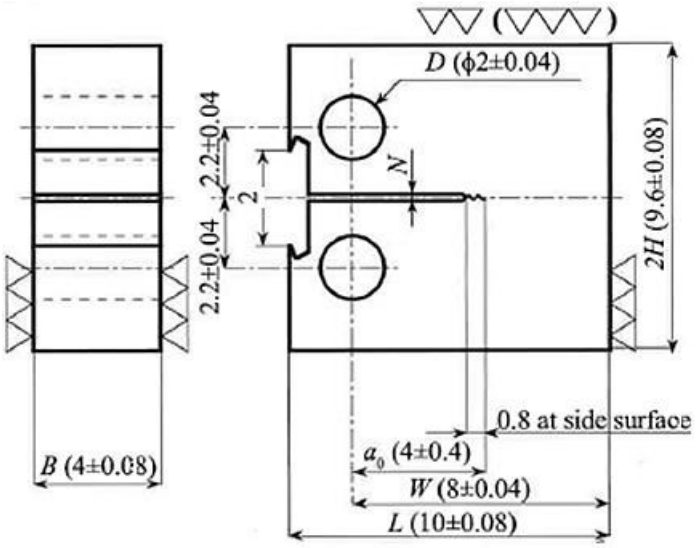

Figure 33 Dimensions of a miniature size C(T) specimen.

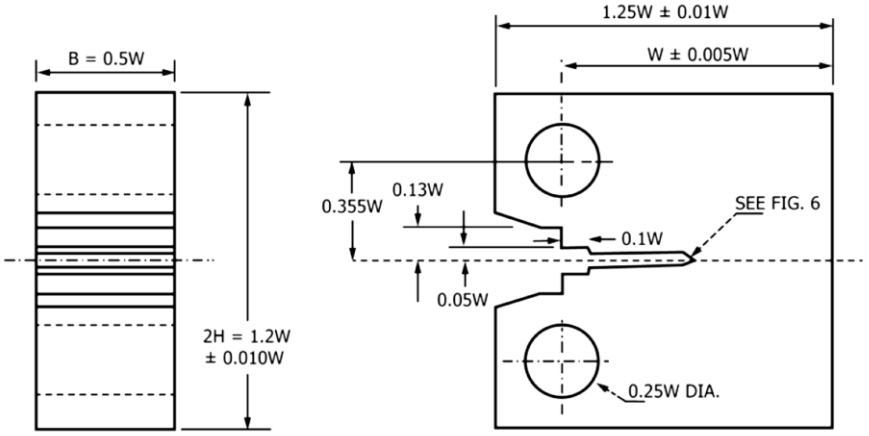

Figure 34 Size of a C(T) specimen according to ASTM E1820.
(ASTM E1820, 2015)

3.3.2 Manufacturing of specimens

Manufacturing of a miniature size specimen has some limitations regarding machining; practically the only feasible way is to use an electric discharge machine (EDM) which enables required accuracy. Process is based on using electric discharge between tool and workpiece immersed in a dielectric liquid. In Figures 35-36 is presented cutting schemes of miniature specimens from Barsebäck 2 material and in Figures 37-38 from Ringhals 4 surrogate weld metal.

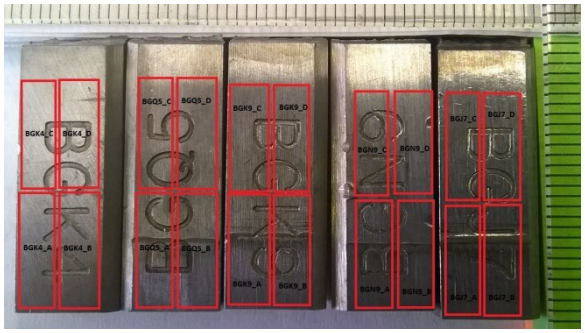

Figure 35 The cutting scheme of Barsebäck 2 material.

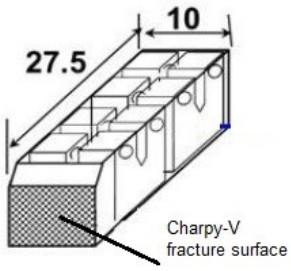

Figure 36 The direction of notches. (Japan Atomic Energy Agency, 2017)

The Barsebäck 2 material consists of tested Charpy-V notch specimen halves and miniature specimens were cut so, that the notch was parallel to fracture surface of Charpy-V notch specimen, as seen in Figure 36.

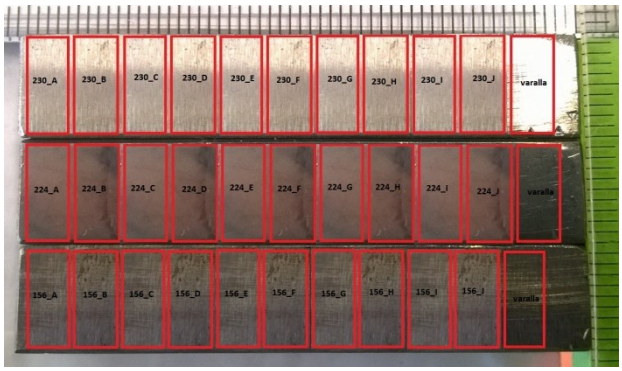

Figure 37 The cutting scheme of Ringhals 4 surrogate weld metal.

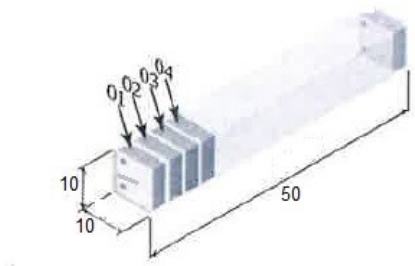

Figure 38 Specimens cutting direction. (Modified) (Yamamoto et al., 2015)

The Ringhals 4 surrogate weld metal test specimens were cut in the opposite way, since CVN specimens were in full length, not tested specimen halves, as Barsebäck 2 material. Therefore, the direction of notches was not essential.

3.4 Methodology of ASTM E1921

According to ASTM E1921: "This test method covers the determination of a reference temperature, T_0, which characterizes the fracture toughness of (macroscopically homogeneous) ferritic steels that experience onset of cleavage cracking at elastic, or elastic-plastic K_{Jc} instabilities, or both". However, as a complement to previous; RPV weld metals are acknowledged as homogeneous materials. (IAEA-TECDOC-1631, 2009)

The test machine, test specimens as well as the preparations and equipment are equal to standard method ASTM E1820. Discrepancies concentrate on the test method and analysing phase. In ASTM E1820, the procedure was executed through a compliance method to define fracture toughness. In ASTM E9121, the test is executed by a quasi-static loading rate and the intention is to determine the transition temperature T_0 where median fracture toughness is 100 MPa√m. (ASTM E1921, 2015)

3.4.1 Test method

To begin with the test procedure, at least six specimens must be tested; either bend specimens or compact tension specimens presented in chapter 2.6.1. As mentioned, the loading is executed by quasi-static rate, monotone displacement control. The specimen is loaded until full fracture or partially fractured; at least 20 % of a load drop occurs. The tests are carried out at a constant temperature close to an estimated T_0 temperature. For determining an initial test temperature only appropriate way is usage of constants based on CVN data. Table and further details can be found in ASTM E1921. More knowledge of test arrangements can be found in chapter 4. (McCabe et al., 2005)

3.4.2 Analyses

The toughness data obtained, must be converted for corresponding to (standard 1T) the specimen of 25.4 mm of thickness by Eq. 8. This ensures all data to be acceptable and comparable regardless of the size of the test specimen.

$$K_{Jc(1T)} = K_{min} + \left(K_{Jc(B)} - K_{min}\right)\left(\frac{B}{25.4}\right)^{1/4} \tag{8}$$

where:

$K_{Jc(1T)}$	is K_{Jc} for a specimen size 1T [MPa√m]
K_{min}	is threshold toughness [MPa√m]
$K_{Jc(B)}$	is K_{Jc} for a specimen size B [MPa√m]
B	is specimen thickness [mm]

K_{min}, a deterministic constant of the Weibull distribution, is set to 20 MPa√m based on earlier studies.

Cleavage fracture occurs by a weakest-link mechanism (due to the specific characteristics of the micromechanism of cleavage fracture); therefore the weakest-link theory is applied to a three-parameter Weibull distribution of fracture toughness. Eq. 9 gives the Weibull scale parameter (Weibull mean toughness), K_o, at the test temperature:

$$K_o = \left[\sum_{i=1}^{N} \frac{\left(K_{Jc(i)} - K_{min}\right)^4}{N}\right]^{1/4} + K_{min} \tag{9}$$

where:

K_o is K_{Jc} value that presents the 63 percentile level of a K_{Jc} data distribution [MPa√m]
$K_{Jc(i)}$ is either a valid K_{Jc} or censored value [MPa√m]
K_{min} is threshold toughness [MPa√m]
N is the number of valid tests in the data set

Using of Eq. 9 requires toughness values to be converted such as in Eq. 8.

The standard deviation of the data distribution is a function of Weibull slope and median fracture toughness K_{Jc}. They are related by the following formula:

$$K_{Jc(med)} = K_{min} + (K_o - K_{min})[ln(2)]^{1/4} \tag{10}$$

where:

$K_{Jc(med)}$ is median fracture toughness [MPa√m]
K_{min} is threshold toughness [MPa√m]
K_o is K_{Jc} value that presents the 63 percentile level of a K_{Jc} data distribution [MPa√m]

Finally, by rearranging preceding Eq. 2 in chapter 2.4, computing of the transition temperature T_0 occurs subsequently:

$$T_0 = T - \left(\frac{1}{0.019}\right) ln\left[\frac{K_{Jc(med)} - 30}{70}\right] \tag{11}$$

where:

T_0 is reference temperature [°C]
T is test temperature [°C]
$K_{Jc(med)}$ is median fracture toughness [MPa√m]

Eq. 11 holds true for testing at one particularly temperature; Eq. 12 applies for multiple temperatures testing, such as made in this thesis.

$$\sum_{i=1}^{N} \delta_i \frac{\exp\left[0.019\left(T_i - T_{0Q}\right)\right]}{11.0 + 76.7\exp\left[0.019\left(T_i - T_{oQ}\right)\right]} - \sum_{i=1}^{N} \frac{(K_{Jc(i)} - 20)^4 \exp[0.019\left(T_i - T_{0Q}\right)]}{\{11.0 + 76.7\exp[0.019(T_i - T_{0Q})]\}^5} = 0 \quad (12)$$

where:

N	is the number of specimens tested
δ_i	is Kronecker delta; either one (test ended with cleavage fracture) or zero (test ended with ductile fracture mode)
T_i	is test temperature corresponding to $K_{Jc(i)}$ [°C]
T_{0Q}	is provisional T_0 value [°C]
$K_{Jc(i)}$	is either valid K_{Jc} or censored value [MPa√m]
11.0	is approximation of $10(\ln 2)^{1/4}$ MPa√m to 3 significant digits
76.7	is approximation of $70(\ln 2)^{1/4}$ MPa√m to 3 significant digits

As mentioned, the Master Curve method works best in the ductile-brittle transition region. In addition, the lower shelf region is acceptable for applying the Master Curve method, though data may not fit very well. However, when approaching to ductile tearing and upper shelf, Master Curve method becomes unsuitable. (Anderson, 2005; McCabe et al., 2005; IAEA-TECDOC-1631, 2009; ASTM E1921, 2015)

3.5 Metallographic characterisation

3.5.1 Fractography

Fractographic examinations among with metallographic techniques are being used to determine the crack path with relation to microstructure of a component. Any discontinuities may influence the crack path and in the end, microstructure specifies whether the path is intergranular or transgranular. Fractographic examination offers facts as well from metallurgical condition of the material; thermomechanical treatment can be interpreted from the grain size and shape (Hertzberg et al., 2013). The light microscope has two basic elements: optical and illumination systems and disparate regions of the microstructure reflect differently producing contrasts in the image. Such types of examinations are called metallographic. (Callister, 2007)

Characterisation of the texture of the fracture surface is a part of fractographic examination; markings of different degrees may indicate particular fracture mechanism (Hertzberg et al., 2013). In Figure 39 is a view, taken with an optical microscope, from the surface of cleavage fracture; common features such as shiny, grainy and flat textures are visible.

Figure 39 Image of fracture surface taken by an optical microscope.

The variation of different colour tones is due to the heating in a furnace; this facilitates the visual examination of surface and separates different areas brighter, e.g. fatigue pre-crack, cleavage fracture and final rupture.

3.5.2 Characterisation of the crack origin

Locating of the crack origin is the utmost important matter to begin with, subsequently identified whether there are one or more fracture initiation sites and their locations. Often the fracture surface shows contour lines pointing back at the crack origin; by following such features one may locate the region where the crack had formed or pre-existed. It is possible for crack to initiate by one mechanism but to propagate by another mechanism; these changes of mechanism may be identified by changes in texture of the fracture surface. (Hertzberg et al., 2013)

The following image, Figure 40, is taken with a scanning electron microscope (SEM) which enables sample viewing directly in the instrument. Magnification ranging up to excess of 50 000 times and vast depths of field enable accurate examination of the fracture surface. The surface is scanned with an electron beam, and the reflected beam of electrons is collected, and then displayed on a cathode ray tube (Callister, 2007).

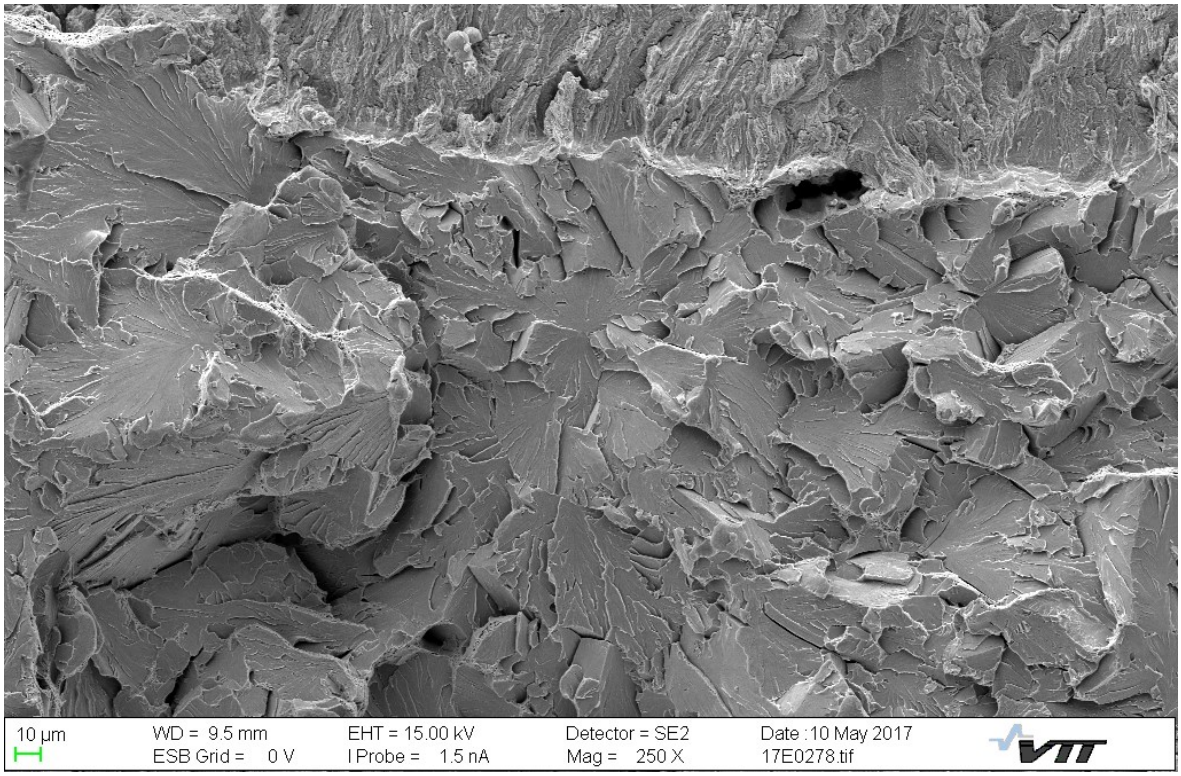

Figure 40 SEM image of cleavage fracture surface.
(Lydman et al., 2017)

In Figure 40 is an exemplary image of the crack origin; cleavage is directed towards the crack origin and crack has propagated fan-shaped around the origin. In Figure 41 is a sketch of common initiation behaviour in the ductile-brittle transition region. A characteristic location for cleavage fracture initiation is in front of the fatigue pre-crack alongside the crack frontal (Wallin et al., 2016); exactly such as in Figure 41.

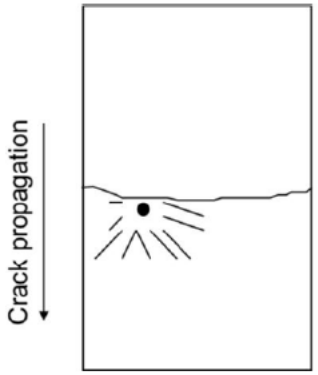

Figure 41 A common initiation site of a crack in the ductile-brittle transition region.
(Wallin et al., 2016)

4 Experimental research

Experimental research chapter includes description of T_0-testing facilities, preparation of specimens and testing in practise.

4.1 Experimental arrangements

A common way to execute fracture toughness testing is to use servo-hydraulic material testing machines. The capacity of a testing machine can vary depending on a test specimen size and a load needed for testing. Some general apparatus loads are up to 50 kN, 100 kN and 250 kN.

4.1.1 Clevises and bend testing fixture

Test specimens, represented in chapter 3.4.1, require different types of mountings. CT-specimens are loaded by using a pin and a clevis fixture, as presented in Figure 42. The fracture surface displacement mode is opening and the specimen arms rotate open as the load is applied. It is recommended that clevises should be made from ultra-high strength steels and the hardness should be 40 HRC or more. (McCabe et al., 2005; ASTM E1820, 2015)

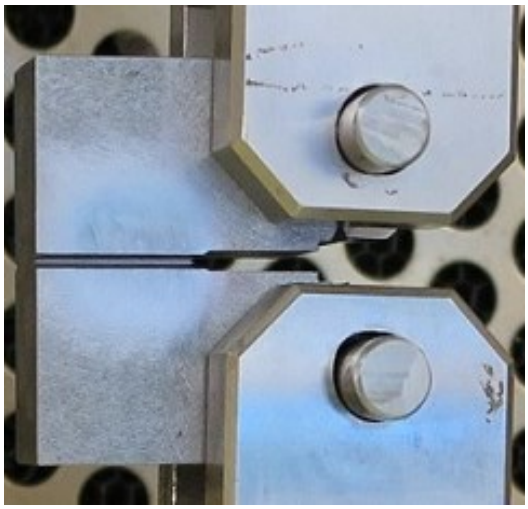

Figure 42 CT-specimen attached to a clevis.

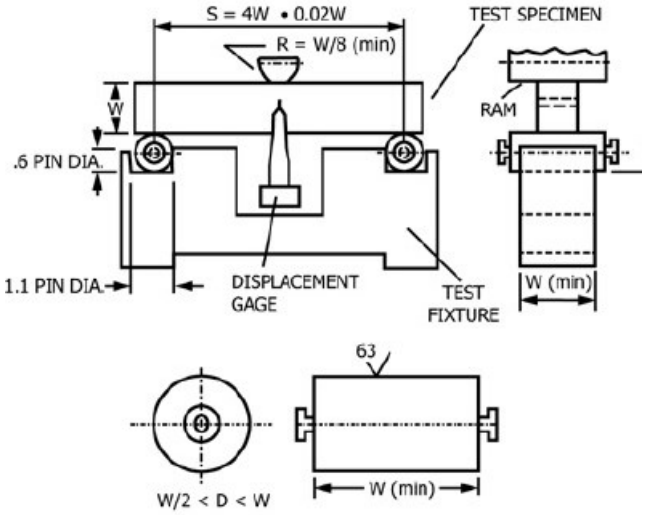

Figure 43 A fixture for bend testing. (ASTM E1820, 2015)

In Figure 43 is presented an illustrative graphic from a three-point bend test fixture. The supporting rollers are able to rotate and move apart slightly when the specimen is loaded. This minimizes frictional effects. The same recommendation from high-hardness steel concerns also the fabrication of the bend-test fixture and rolls. (ASTM E1820, 2015)

4.1.2 Specimen preparation

Fatigue pre-cracking of specimen is the primary step and it needs to be done properly. The most preferable way is to use load-controlled machines; the accuracy and the control are better. A minimum depth of the pre-crack amounts 5 % of the initial crack size. 1 - 2 x 10^5 cycles is the anticipated time for the fatigue of a specimen size of 25 mm in thickness.

According to ASTM E1820, *a/W* shall be between 0.45 and 0.7; also an equation for calculating a force needed for fatigue pre-cracking is found in ASTM E1820. (ASTM E1820, 2015; McCabe et al., 2005)

In Figure 42, in the middle of the specimen, is a side-groove. The purpose of the side-groove is to lead crack propagation and to avoid shear lips; instead of a flat crack surface it may form a U-shape surface. The size of the side-groove is 20 % of specimen thickness; 10 % per side. The fatigue pre-cracking is done initially in order to produce straight as possible fatigue pre-crack front and because visibility is restricted on the basis of the side-groove.

4.1.3 Crack-Opening Displacement (COD) gage

The purpose of COD gage is to measure crack opening during the fracture toughness test. A linear working displacement range depends on the size of the specimen. The range varies between 2 mm and 12 mm, though it can be modified as desired. ASTM E1820 recommends the gage to have a working range not more than twice the displacement to be expected during the test. An operational principle is strain gages inside the COD, but gages used at elevated temperatures are based on capacitive sensors. In Figure 44 is a strain-gage device presented.

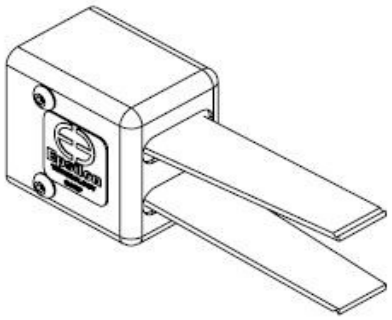

Figure 44 Crack-Opening Displacement (COD) gage. (Epsilon Tech, 2017)

Appearance is similar to both gage functions, except for the variation in method of measurement. The fracture mechanics clip-on gages, such as in Figure 44, are resourced with a self-temperature compensating ability and the range of use which can be varied from -269 °C to +200 °C or even higher.

In CT-specimens, COD gage is attached mostly in the specimen load-line (specimen load-line on distance *W*, Fig. 33), though front face of the specimen is also acceptable. In the latter case, the gage is attached to the specimen front face and gauging is multiplied with a factor to equate load-line attach (McCabe et al., 2005).

4.2 T_0-testing

The arrangements for T_0-testing, regarding particularly this thesis, are presented herein, whereas main principles of ASTM E1921 were described in chapter 3.4.

All specimens were pre-fatigued under load control prior to T_0-testing to an *a/W* ratio of 0.5. However, side grooving was left out from specimens, since studies (Wallin et al., 2016) have proved side grooves to have insignificant effect on fracture toughness results in miniature specimens particularly. The tests were executed with a servo-hydraulic material testing machine with a loading capacity of 50 kN. As a consequence of the size of miniature specimens, special tools were provided to enable execution of demanding tests. Due to the nature of T_0-testing, which requires a reduced temperature, tests were made in an environmental chamber. The reduced temperature was achieved by liquid nitrogen which evaporates inside the chamber. Prior to actual tests in low temperature some extra specimens were tested in room temperature, see Figures 45- 47, in order to confirm the operation of test arrangements.

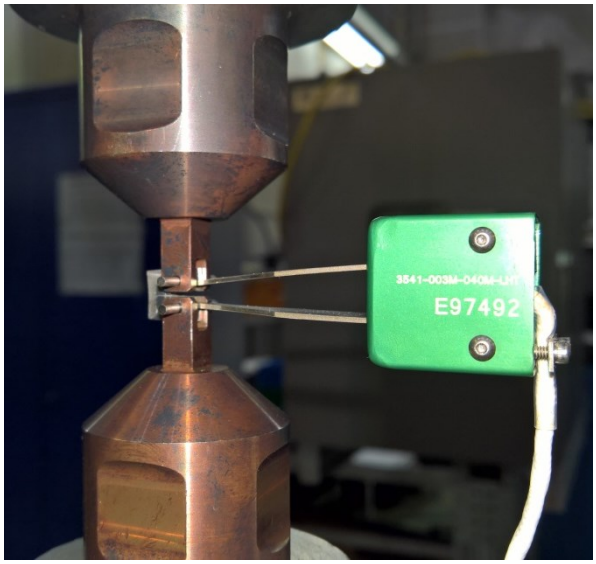

Figure 45 The miniature specimen attached to clevises.

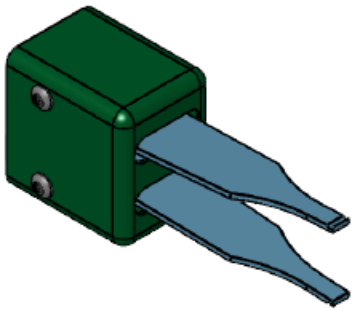

. Figure 46 A modified narrow shaft COD gage (Epsilon Tech, 2017)

The COD clip was engaged to the front face of the specimen (Figure 45) due to the size of the specimen; moreover, the COD gage was modified with narrowed shafts (Figure 46).

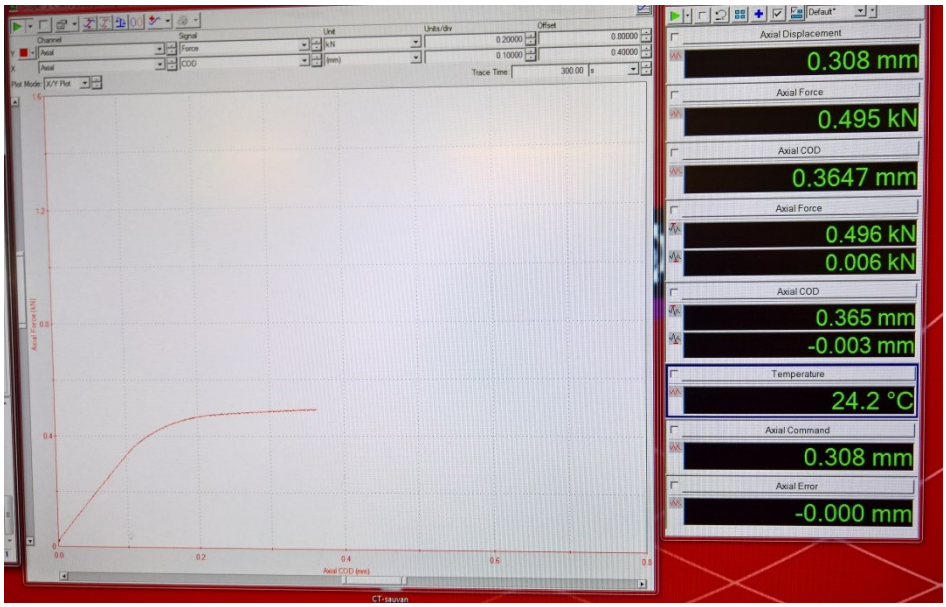

Figure 47 A plot of a test data recorded.

During the tests all data was recorded; axial direction displacement, load and COD with temperature, see Figure 47.

The specimens were loaded by monotonic displacement control until full fracture occurred and hence, unlike when pre-fatigued, load control is infeasible way to operate. When the specimen cracks under load control, there will not be any response for servo valve and it may well cause failures to the specimen, tools or the test machine. Subsequently, tested specimens were held in denatured alcohol until temperature become steady at room temperature level; this prevents any corrosion which would later impede examination of the fracture surface.

5 Results of Barsebäck 2 material and Ringhals 4 surrogate weld metal

The characterisation of microstructure, hardness measurement data, initial crack size with initiation sites, and characterisation of fracture surface together with T_0-temperatures are presented herein.

The microstructural examinations of Barsebäck 2 material revealed variations in consistency; presumed weld metal included three different microstructures which were base material, heat affected zone and weld metal. Table 4 shows these different consistencies of specimens studied from Barsebäck 2 material. Henceforth, the material from Barsebäck 2 NPP is referred to as Barsebäck 2 material, since expression covers all different microstructures.

Table 4. Consistencies of specimens from Barsebäck 2 material.

Specimen ID	Consistency
BGK9.1	base material
BGK9.2	base material
BGK9.3	weld metal
BGK9.4	weld metal
BGN9.2	weld metal
BGN9.3	base material
BGN9.4	base material
BGJ7.1	base material
BGJ7.2	haz
BGQ5.1	haz
BGQ5.2	base material

5.1 Characterisation of microstructure

In order for the characterisation of microstructure, a metallographic sample from each material was prepared. The sample was polished and etched with Nital (2 to 3 % ethanol-nitric acid solutions) with an intention to reveal the ferrite grains. In Figure 48 is presented the microstructure of the Ringhals 4 surrogate weld metal, specimen 224.1 and in Figure 49 is the microstructure of the Barsebäck 2 material, specimen BGN9.2 with five different magnifications: 2.5x, 10x, 20x, 50x and 100x.

In Figure 48 an overall appearance of the microstructure is bainite and some ferrite in it; bainite is coarse lath-like upper bainite, whereas light areas represent ferrite, possibly polygonal.

In Figure 49 the dominant microstructure is ferritic with observable bainitic regions which consist of upper and lower bainite. Grain boundary ferrite appears in long and narrow, light phases; between grain boundary ferrite lines is acicular ferrite in sight. Acicular ferrite can be seen particularly near the crack initiation site (square figure).

Assessment of the materials grain size was made in accordance of SFS-EN 643 Steels – Micrographic determination of the apparent grain size (SFS Standards Publication, 2012) by comparison with standard grain size charts. Commonly the grain size is characterised by an index G and the index is defined by the following formula:

$$m = 8 \times 2^{G} \tag{13}$$

where:

m is number of grains per square millimetre of test piece surface in the area examined

The assessment was done by comparison with standard grain size charts; the image examined on the microscope is compared with a series of standard charts at a magnification of 100x. The standard charts are numbered from 00 to 10 so that their number equals to the index G. The grain size determination was done to specimens 224.1 of the Ringhals 4 surrogate weld metal and BGK4.1 of the Barsebäck 2 material. Table 5 shows the index G and the number of grains per mm^2.

Table 5. Grain size index and number of grains per mm^2.

Material	Index G	Number of grains per mm^2 m
B2	4-5	128 - 256
R4	7-8	1024 - 2048

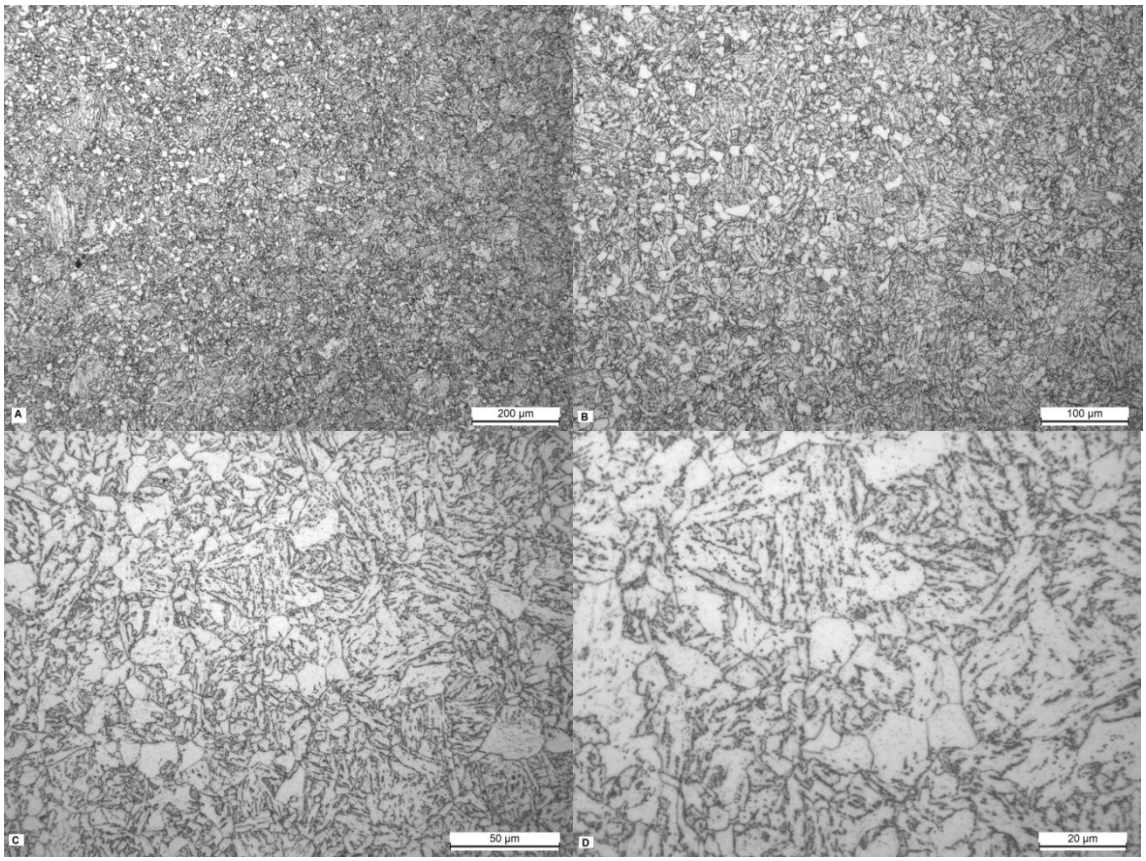

Figure 48 Microstructure of the 224.1 (R4) with magnification of a) 10x, b) 20x, c) 50x and d) 100x.

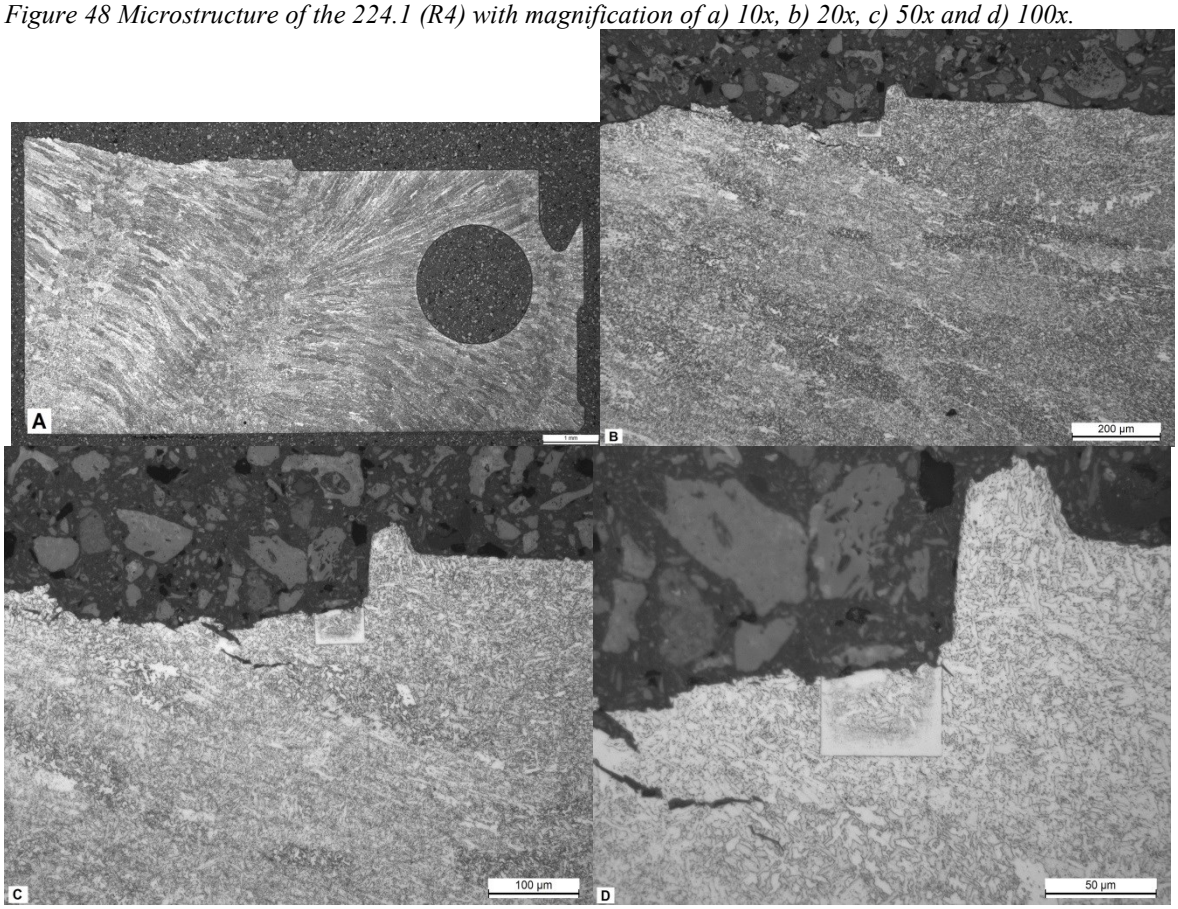

Figure 49 Microstructure of the BGN9.2 (B2) with magnification of a) 2.5x, b) 10x, c) 20x and d) 50x (Lydman et al., 2017)

5.2 Hardness measurement

One specimen of each material, Barsebäck 2 material and Ringhals 4 surrogate weld metal was measured to obtain the HV1 hardness (Tables 6 and 7). The specimen BGJ7.2 represents the Barsebäck 2 material and the hardness was measured from three different areas; around base material, HAZ and weld metal, see Figure 50. The specimen 224.1 of Ringhals 4 surrogate weld metal was measured around the fatigue pre-crack region, see Figure 51.

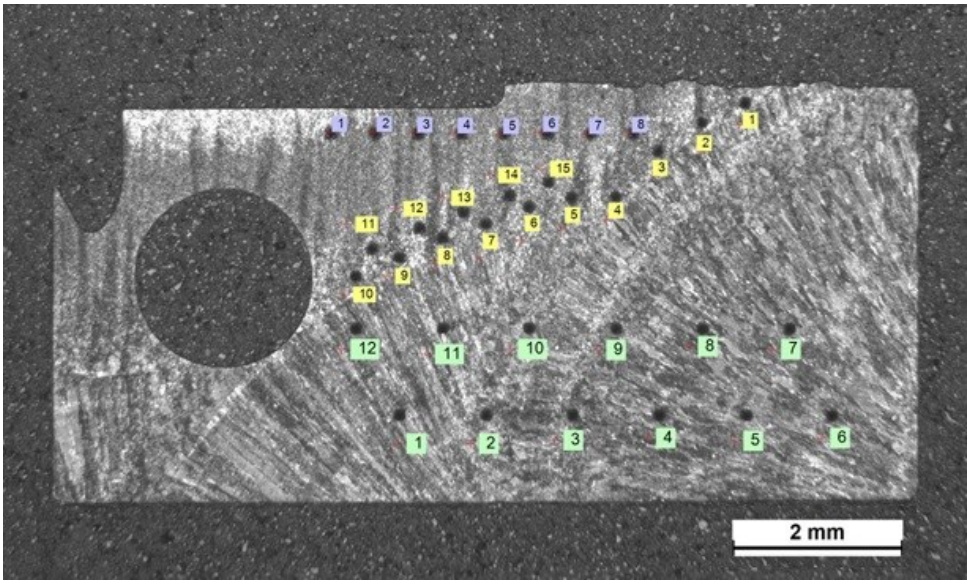

Figure 50 Locations of the hardness measurements in Barsebäck 2 material; numbers in purple indicate the base material, in yellow the HAZ area and in green the weld metal.

Table 6. Hardness measurements of Barsebäck 2 material.

Material	Specimen	Hardness HV	Number of measuring point	Area
B2	BGJ7.2	160	1	Base material
B2	BGJ7.2	178	2	Base material
B2	BGJ7.2	172	3	Base material
B2	BGJ7.2	188	4	Base material
B2	BGJ7.2	185	5	Base material
B2	BGJ7.2	176	6	Base material
B2	BGJ7.2	182	7	Base material
B2	BGJ7.2	209	8	Base material
B2	BGJ7.2	205	1	haz
B2	BGJ7.2	240	2	haz
B2	BGJ7.2	222	3	haz
B2	BGJ7.2	238	4	haz
B2	BGJ7.2	219	5	haz
B2	BGJ7.2	203	6	haz
B2	BGJ7.2	209	7	haz
B2	BGJ7.2	204	8	haz

B2	BGJ7.2	210	9	haz
B2	BGJ7.2	247	10	haz
B2	BGJ7.2	223	11	haz
B2	BGJ7.2	197	12	haz
B2	BGJ7.2	186	13	haz
B2	BGJ7.2	219	14	haz
B2	BGJ7.2	211	15	haz
B2	BGJ7.2	214	1	Weld metal
B2	BGJ7.2	210	2	Weld metal
B2	BGJ7.2	210	3	Weld metal
B2	BGJ7.2	214	4	Weld metal
B2	BGJ7.2	214	5	Weld metal
B2	BGJ7.2	211	6	Weld metal
B2	BGJ7.2	212	7	Weld metal
B2	BGJ7.2	214	8	Weld metal
B2	BGJ7.2	209	9	Weld metal
B2	BGJ7.2	216	10	Weld metal
B2	BGJ7.2	220	11	Weld metal
B2	BGJ7.2	211	12	Weld metal

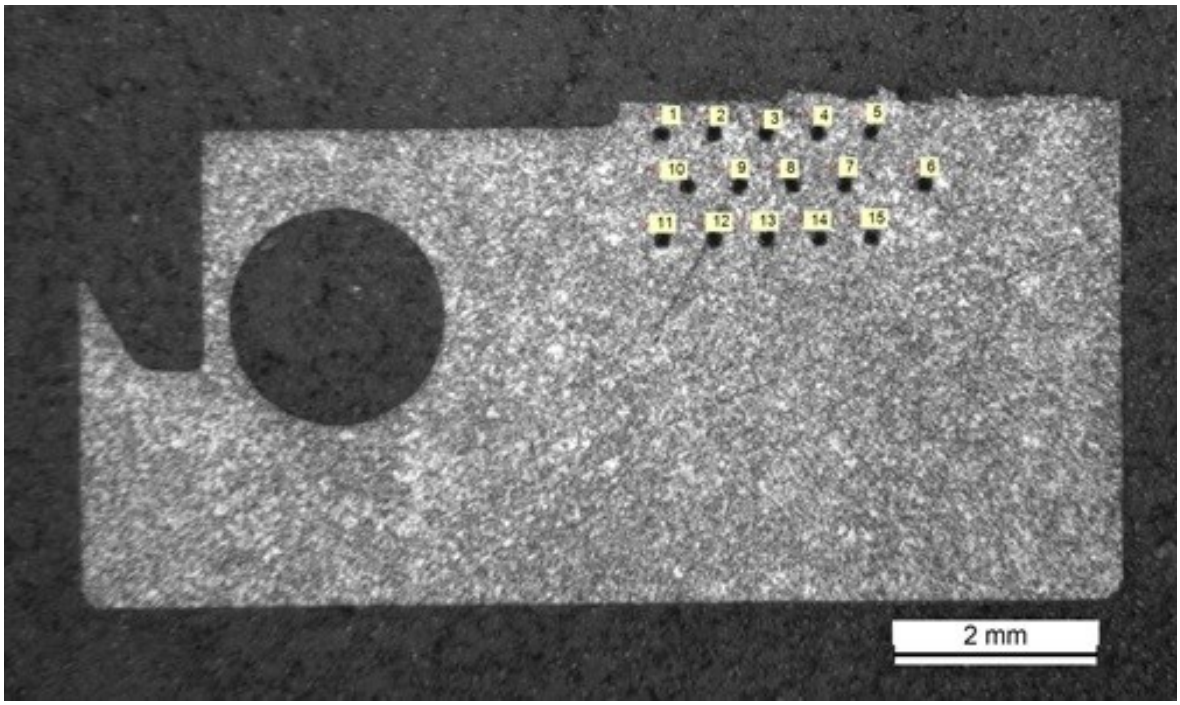

Figure 51 Locations of hardness measurements of Ringhals 4 surrogate weld metal.

Table 7. Hardness measurements of Ringhals 4 surrogate weld metal.

Material	Specimen	Hardness HV	Measuring point
R4	224.1	176	1

R4	224.1	193	2
R4	224.1	209	3
R4	224.1	182	4
R4	224.1	176	5
R4	224.1	187	6
R4	224.1	176	7
R4	224.1	200	8
R4	224.1	185	9
R4	224.1	199	10
R4	224.1	185	11
R4	224.1	192	12
R4	224.1	181	13
R4	224.1	192	14
R4	224.1	176	15

The average hardness of Barsebäck 2 materials base material was 177 HV and the standard deviation was 9 HV. The eighth measuring point was left out, since it located too near to the HAZ region and measured value was elevated comparing to other base material values. The average hardness of Barsebäck 2 material HAZ area was 216 HV and the standard deviation was 17 HV when the standard deviation of Barsebäck 2 material weld metal was 3 HV and the average hardness was 213 HV.

The average hardness of Ringhals 4 surrogate weld metal was 187 HV with standard deviation of 10 HV. In both, Barsebäck 2 material and Ringhals 4 surrogate weld metal, standard deviations were relatively small. Both measured specimens were tested in -130 °C. Table 8 presents hardness measurement results.

Table 8. Average and standard deviation of hardness measurements.

Material	Average HV	Standard deviation HV
B2 base material	177	9
B2 weld metal	213	3
B2 haz	216	17
R4 surrogate weld metal	187	10

5.3 Initial crack size

Initial crack size a_0 represents the specimens crack size in its entirety in the case of cleavage fracture, since cleavage fracture tends to initiate at the fatigue pre-crack tip. The ASTM E1921 sets requirement for initial crack length a_0 to be within $0.5W \pm 0.05W$; Table 9 indicates that four specimens of Barsebäck 2 material exceeded the limit, whereas all specimens from Ringhals 4 surrogate weld metal were between limit 3.6 – 4.4 mm.

For Barsebäck 2 material specimens that exceeded the set limit and consequently the initial crack length is longer than the standard requires; this can increase the measured T_0 compared to T_0 determined with an a/W ratio of 0.5. Longer a_0 may be as a consequence of

difficulty to visually estimate the pre-crack size prior to testing or stem from material properties; as-welded weld seam. Latter seems more likely. Moreover, the growth of fatigue pre-crack in weld metals can be unstable as a consequence of residual stresses (Wallin, 2017). The fatigue pre-crack length of all specimens was between *a/W* ratio 0.51 – 0.56.

Table 9. Table of pre-crack lengths.

Material	Specimen	Test temperature °C	Initial crack length a_0
B2	BGK9.1	-120°C	4.404
B2	BGK9.2	-130°C	4.244
B2	BGK9.3	-130°C	4.387
B2	BGK9.4	-130°C	4.367
B2	BGN9.1	-100°C	4.323
B2	BGN9.2	-140°C	4.282
B2	BGN9.3	-140°C	4.285
B2	BGN9.4	-120°C	4.469
B2	BGK4.1	-130°C	4.464
B2	BGJ7.1	-140°C	4.338
B2	BGJ7.2	-130°C	4.380
B2	BGQ5.1	-140°C	4.511
B2	BGQ5.2	-140°C	4.319
R4	156 B	-100°C	4.022
R4	156 C	-100°C	4.096
R4	156 E	-100°C	4.168
R4	156 H	-100°C	4.056
R4	156 I	-100°C	3.972
R4	224.1	-130°C	3.868
R4	224.2	-130°C	4.194
R4	224.3	-130°C	4.030
R4	224.4	-120°C	4.087
R4	224.5	-120°C	4.101
R4	224.6	-80°C	4.064
R4	224.7	-120°C	4.077
R4	224.8	-110°C	3.905
R4	224.9	-90°C	3.892
R4	224.10	-100°C	4.046
R4	230 A	-100°C	3.820

ASTM E1921 has a criterion for the straightness of the fatigue pre-crack front in order for K_{Jc} value to be valid. The standard requires that the maximum deviation of a single crack length from the average (a nine-point measuring procedure, see Figure 26) shall not deviate more than 5% or 0.5 mm from the average crack length; the larger value is selected. Specimens BGK4.1 and BGN9.1 fail the crack front straightness criteria; the fatigue pre-crack was skewed and additionally in the latter specimen slow stable crack growth Δa_p occurred for an amount of 0.84 mm and hence it was categorised as ductile fracture.

In all specimens the estimated fatigue pre-crack length, $a_{0predicted}$, was compared with the optical post-test measured initial crack size, a_0. According to ASTM E1921 the pre-test estimate should not differ more than 5 % of post-test optical value. However, in such case adjusting of the nominal value 210 MPa of E by 10 % is acceptable to equalize the difference. Majority of the specimen $a_{0predicted}$ did not differ over 5 % from a_0, except for specimens 224.4 and 224.9. The value of E of these specimens was adjusted as following: for specimen 224.4 E = 190 GPa and for specimen 224.9 E = 200 GPa; specimen 224.4 still failed to fulfil the criteria.

5.4 Fractography

All tested specimens were visually examined with an optical microscope and a scanning electron microscope (SEM) aiming to characterise the fracture surface; for signs of cleavage or ductile fracture and to identify such characteristic features. The major fracture mode was cleavage fracture and therefore Figures 52-60 from Lydman et al.'s research report (Lydman et al., 2017) show common features of cleavage fracture surface of Barsebäck 2 material (specimen BGN9.2), beginning with magnification of 25x and ending to magnification of 10 000x. In the subsequent images, the blue arrow points to the crack initiation site.

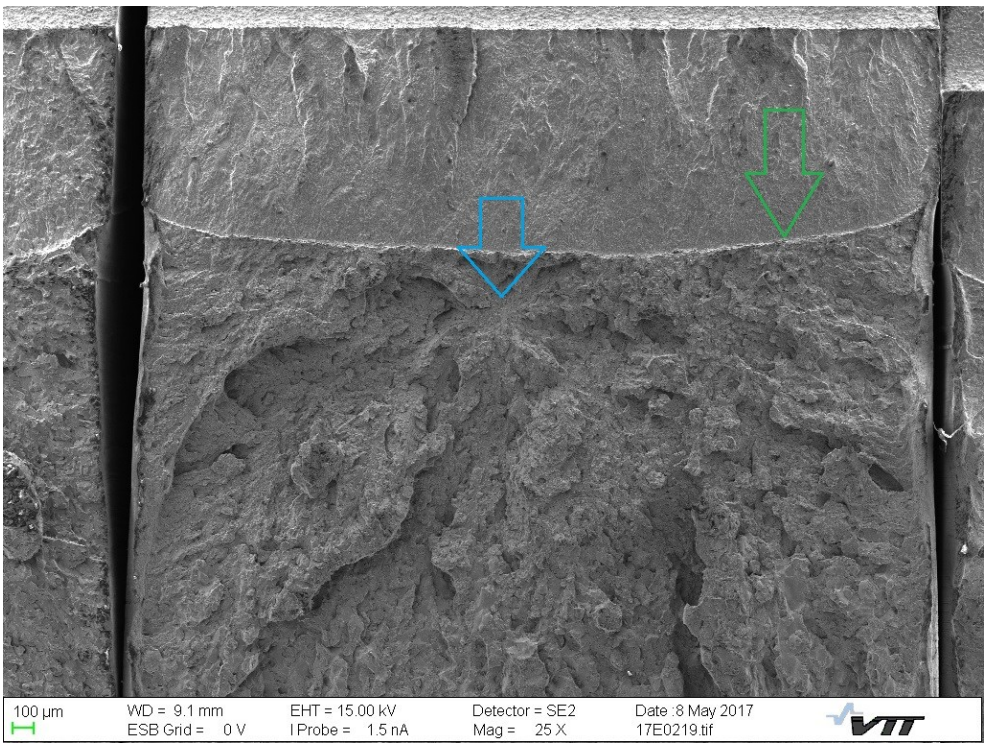

Figure 52 SEM image of cleavage fracture surface with magnification 25x, the blue arrow indicates the initiation site and the green arrow points the fatigue pre-crack tip. (Lydman et al., 2017)

Figure 52 shows the fatigue pre-crack and cleavage fracture.

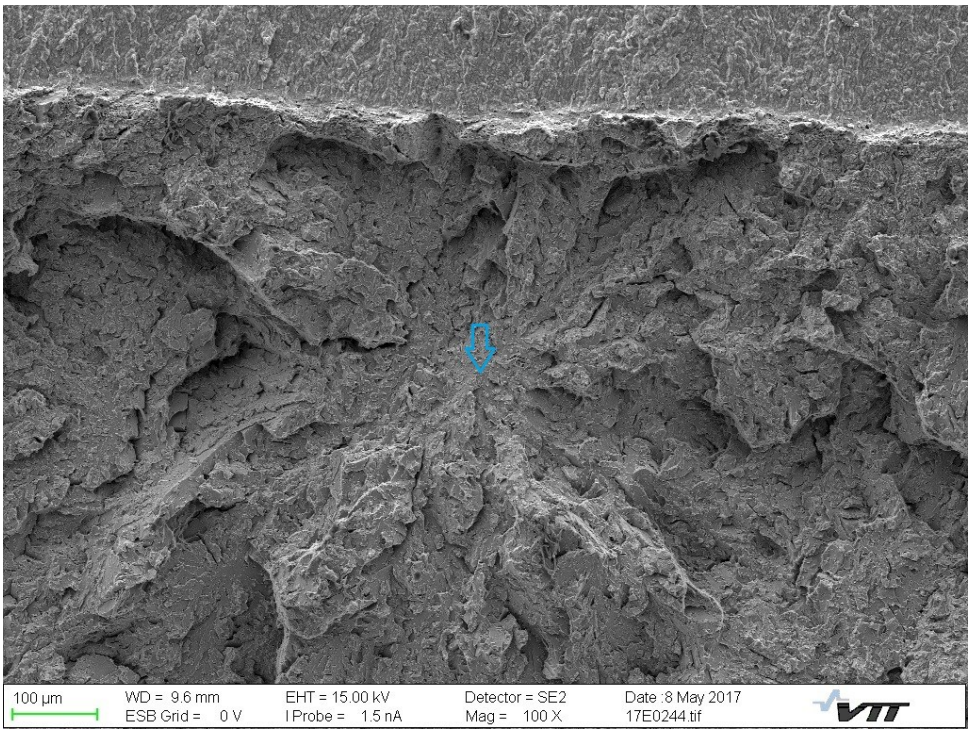

Figure 53 SEM image of cleavage fracture surface with magnification 100x; the blue arrow indicates the initiation site.
(Lydman et al., 2017)

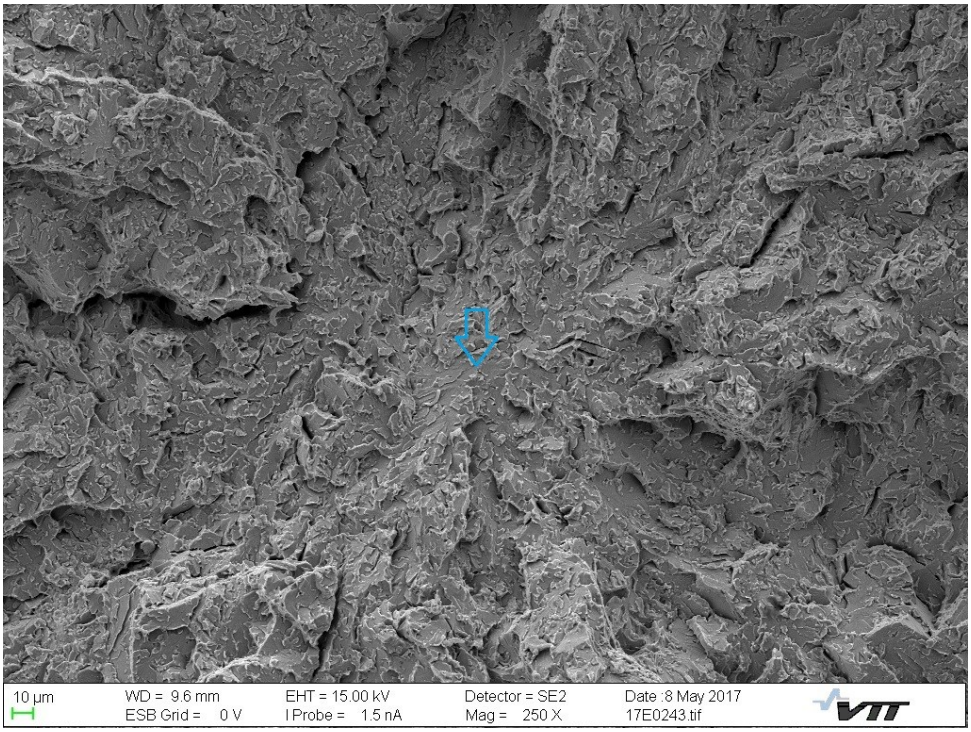

Figure 54 SEM image of cleavage fracture surface with magnification 250x; the blue arrow indicates the initiation site.
(Lydman et al., 2017)

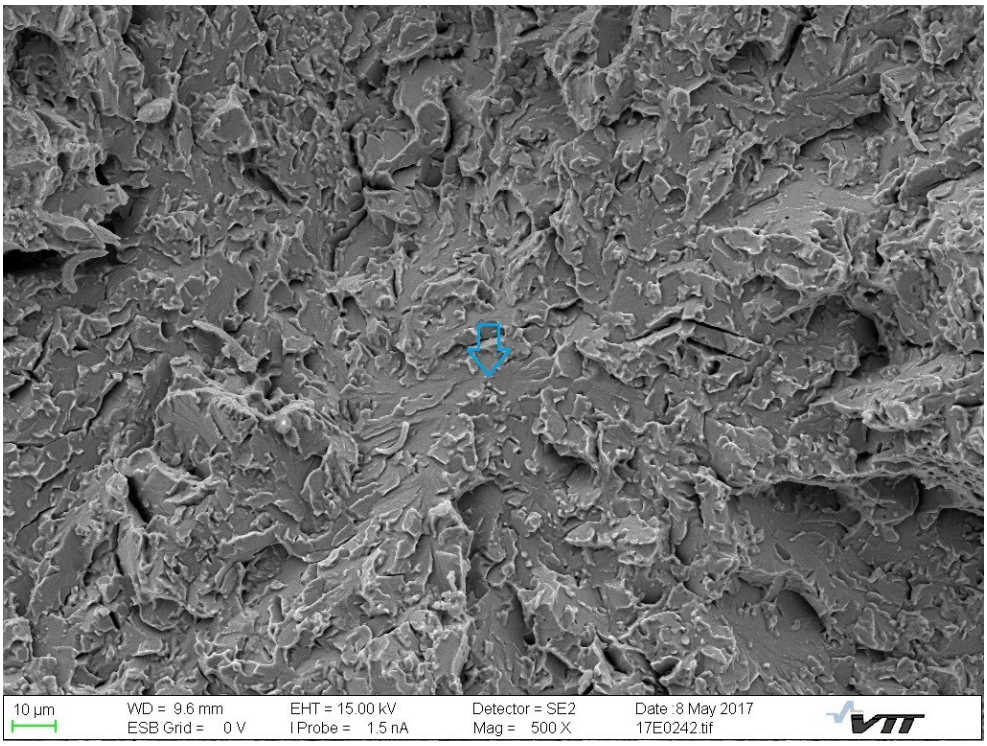

Figure 55 SEM image of cleavage fracture surface with magnification 500x; the blue arrow indicates the initiation site.
(Lydman et al., 2017)

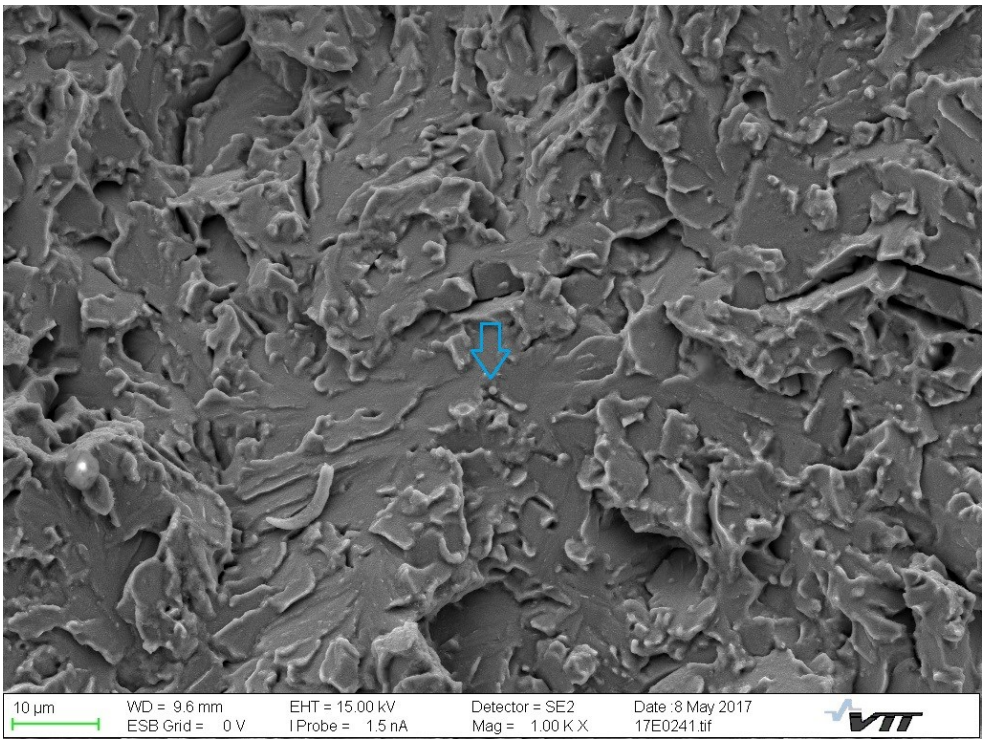

Figure 56 SEM image of cleavage fracture surface with magnification 1000x; the blue arrow indicates the initiation site.
(Lydman et al., 2017)

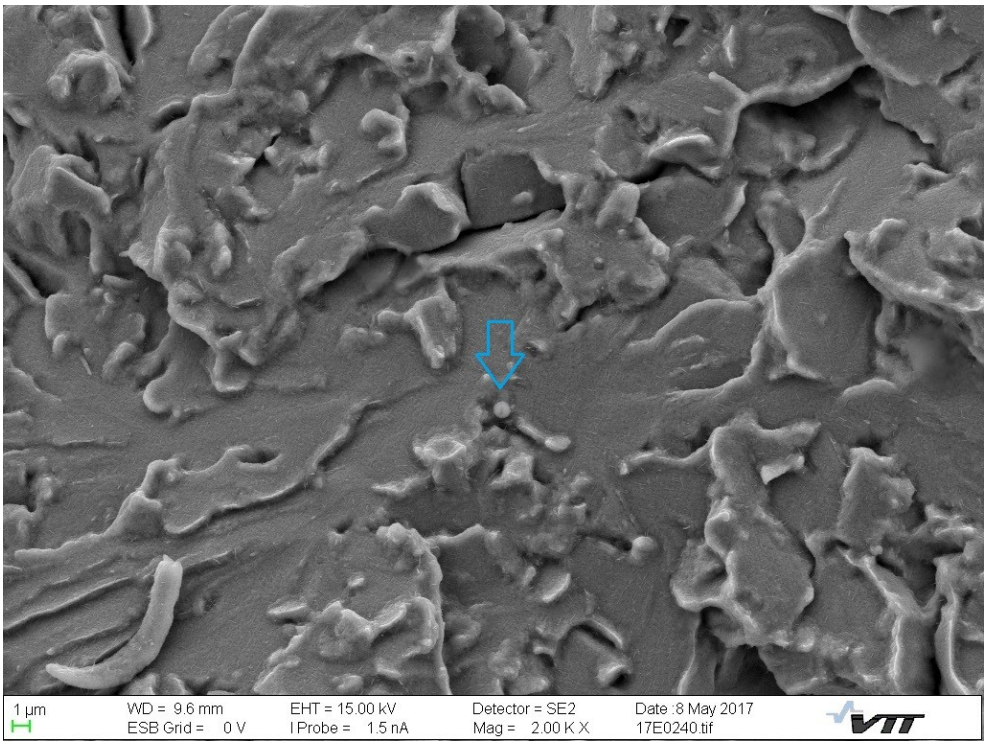

Figure 57 SEM image of cleavage fracture surface with magnification 2000x; the blue arrow indicates the initiation site.
(Lydman et al., 2017)

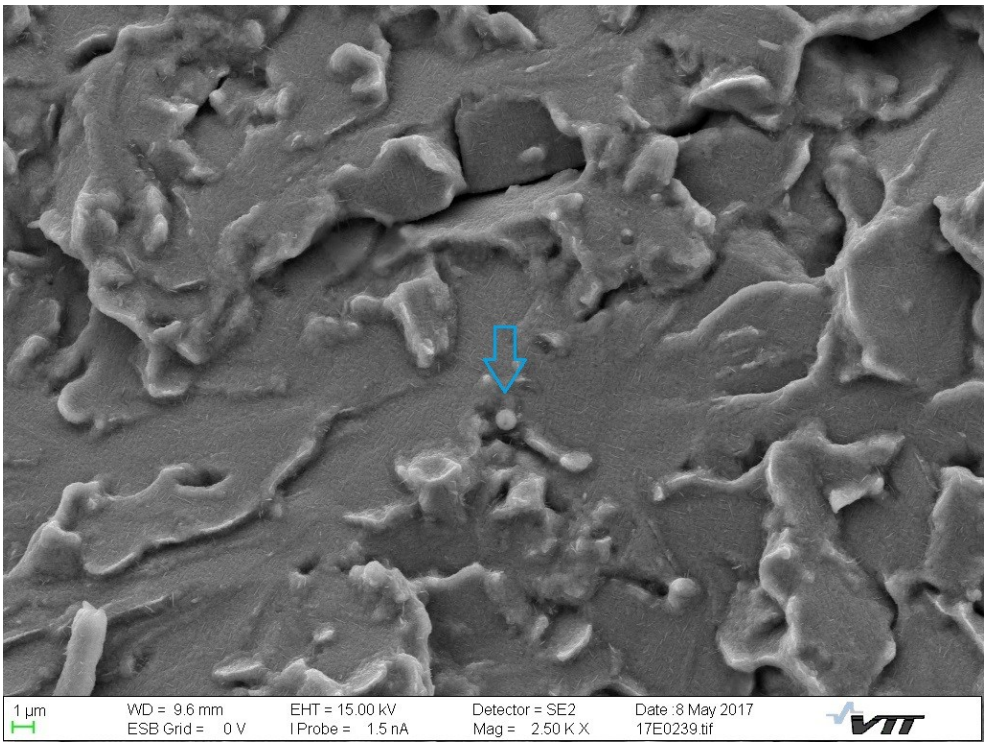

Figure 58 SEM image of cleavage fracture surface with magnification 2500x; the blue arrow indicates the initiation site.
(Lydman et al., 2017)

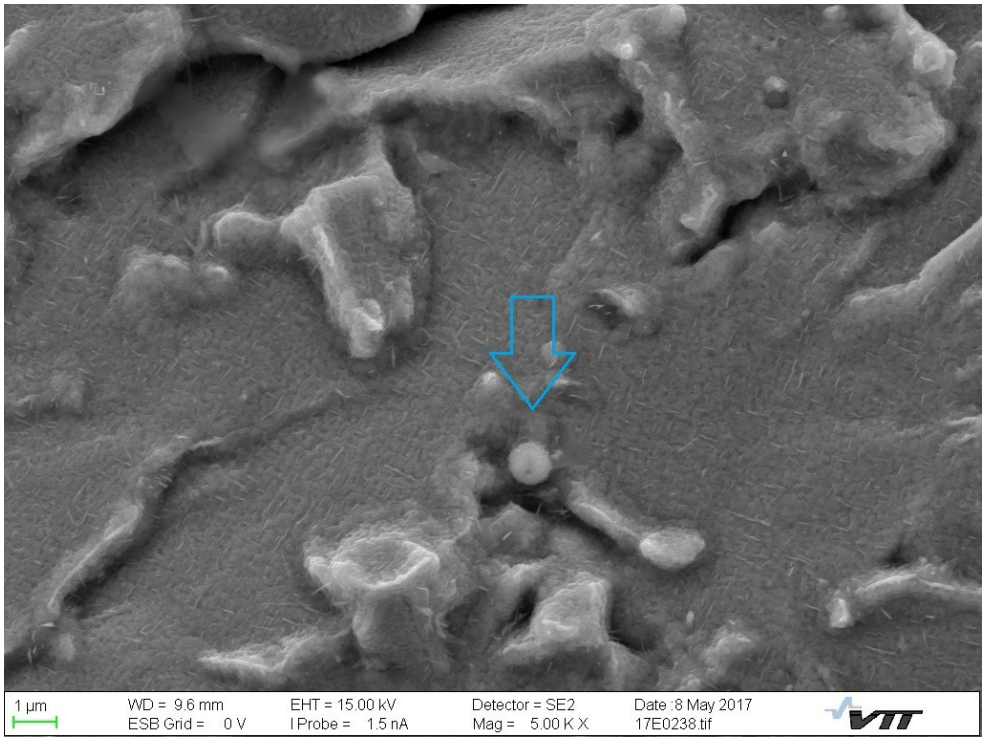

Figure 59 SEM image of cleavage fracture surface with magnification 5000x; the blue arrow indicates the initiation site.
(Lydman et al., 2017)

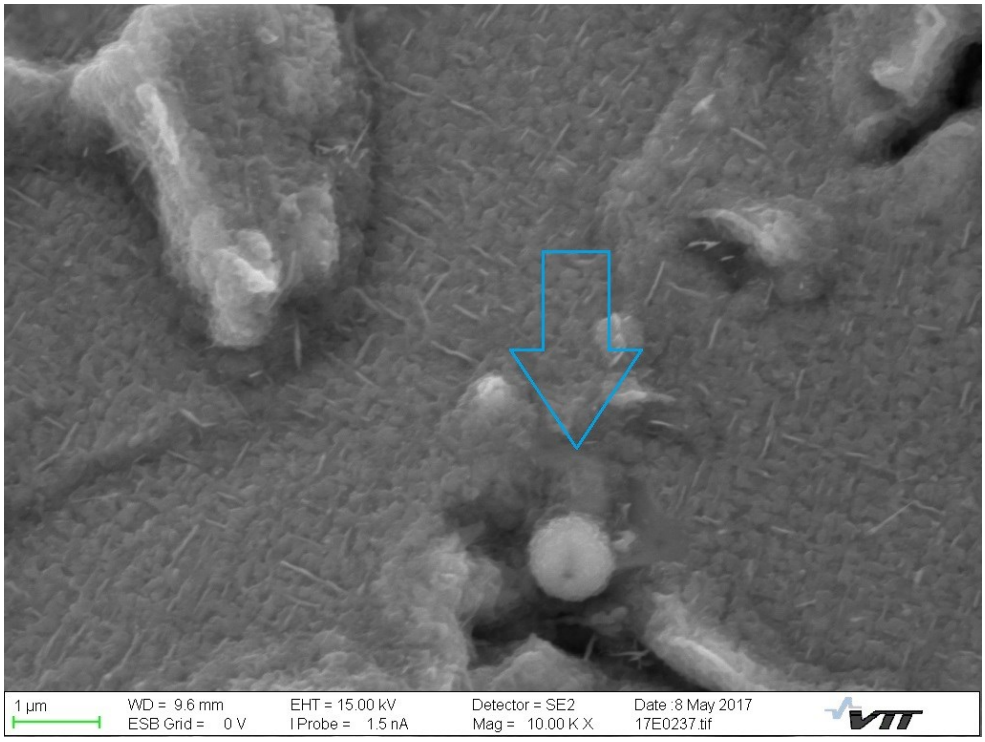

Figure 60 SEM image of cleavage fracture surface with magnification 10 000x; the blue arrow indicates the initiation site, at which the particle seen in the image is Mo-, Mn-, Cu-, S- and Al-rich particle.
(Lydman et al., 2017)

5.5 Initiation sites

The initiation locations respective to the fatigue pre-crack tip are presented in Table 10. The locations were determined qualitatively with SEM.

Table 10. Initiation distances from the fatigue pre-crack tip.

Specimen	The initiation distance from the fatigue pre-crack tip [mm]	Test temperature °C
BGK9.1	0.261	-120
BGK9.2	0.069	-130
BGK9.3	0.054	-130
BGK9.4	0.056	-130
BGN9.2	0.291	-140
BGN9.3	0.055	-140
BGN9.4	0.254	-120
BGQ5.1	0.033	-140
BGQ5.2	0.219	-140
BGJ7.1	0.069	-140
BGJ7.2	0.060	-130

5.6 Transition temperature T_0

Table 11 shows the mechanical properties that were used in determination of the transition temperature T_0. As mentioned in chapter 2.1, bcc microstructure metals have strong yield strength-temperature correlation. Consequently, yield strength σ_{YS} and ultimate tensile strength σ_{TS} were corrected to correspond the test temperature of each specimen with formulas given by the British Standard (Kocak et al., 2008). Eq. 14 is for correction of σ_{YS} and Eq. 15 for σ_{TS}.

$$\sigma_{YS(at\ LT)} = \sigma_{YS(at\ RT)} + \frac{10^5}{(491 + 1.8T)} - 189 \tag{14}$$

$$\sigma_{TS(at\ LT)} = \sigma_{TS(at\ RT)} \times \left(0.7857 + 0.2423 exp\left(-\frac{T}{170.646}\right)\right) \tag{15}$$

where:

$\sigma_{YS(at\ LT)}$ is σ_{YS} at low temperature, between RT and -196°C [MPa]
$\sigma_{YS(at\ RT)}$ is σ_{YS} at room temperature [MPa]
$\sigma_{TS(at\ LT)}$ is σ_{TS} at low temperature, between RT and -196°C [MPa]
$\sigma_{TS(at\ RT)}$ is σ_{TS} at room temperature [MPa]

Table 11. Mechanical properties used in determination of the transition temperature T_0.

Material	Specimen	σ_{YS} MPa	σ_{TS} MPa	Test Temperature °C	$^*\sigma_{YS}$ MPa	$^*\sigma_{TS}$ MPa
B2	BGK9.1	425	573	-120°C	600	730
B2	BGK9.2	425	573	-130°C	625	747
B2	BGK9.3	560	642	-130°C	760	838
B2	BGK9.4	560	642	-130°C	760	838
B2	BGN9.1	560	642	-100°C	693	784
B2	BGN9.2	560	642	-140°C	789	858
B2	BGN9.3	425	573	-140°C	654	765
B2	BGN9.4	425	573	-120°C	600	730
B2	BGK4.1	425	573	-130°C	625	747
B2	BGJ7.1	425	573	-140°C	654	765
B2	BGJ7.2	560	642	-130°C	760	838
B2	BGQ5.1	560	642	-140°C	789	858
B2	BGQ5.2	425	573	-140°C	654	765
R4	156 B	560	642	-100°C	693	784
R4	156 C	560	642	-100°C	693	784
R4	156 E	560	642	-100°C	693	784
R4	156 H	560	642	-100°C	693	784
R4	156 I	560	642	-100°C	693	784
R4	224.1	560	642	-130°C	760	838
R4	224.2	560	642	-130°C	760	838
R4	224.3	560	642	-130°C	760	838
R4	224.4	560	642	-120°C	735	819
R4	224.5	560	642	-120°C	735	819
R4	224.6	560	642	-80°C	659	753
R4	224.7	560	642	-120°C	735	819
R4	224.8	560	642	-110°C	712	801
R4	224.9	560	642	-90°C	675	768
R4	224.10	560	642	-100°C	693	784
R4	230 A	560	642	-100°C	693	784

σ_{YS} = yield strength at room temperature [MPa]
σ_{TS} = ultimate tensile strength at room temperature [MPa]
$^*\sigma_{YS}$ = temperature corrected yield strength used in calculation [MPa]
$^*\sigma_{TS}$ = temperature corrected ultimate tensile strength used in calculation [MPa]

Table 12 shows the test data used in determination of the T_0. For two specimens of Ringhals 4 surrogate weld metal and for one specimen of Barsebäck 2 material, BGN9.1, the test ended with a ductile fracture mode and the K_{Jc} value exceeded the $K_{Jc(limit)}$. For specimen BGK9.1 fracture mode was classified as cleavage regardless of an exceeding of the measuring capacity. Since $K_{Jc(limit)}$ defines the maximum capacity of the specimen,

$K_{Jc(limit)}$ was used in determination of T_0 instead of the measured K_{Jc} value. The $K_{Jc(limit)}$ is related to E and σ_{YS} in the following way:

$$K_{Jc(limit)} = \left(E b_0 \sigma_{YS} / 30 \times (1 - v^2)\right)^{1/2} \quad (16)$$

where:

E	is modulus of elasticity [GPa]
b_0	is specimen ligament, W-a_0 [mm]
σ_{YS}	is specimen yield strength [MPa]
v	is Poisson's ratio

Table 12. Test data used in determination of the transition temperature T_0.

Material	Specimen	Test Temperature °C	$K_{Jc\text{-}4mm}$ MPa√m	$K_{Jc\text{-}25mm}$ MPa√m	δ
B2	BGK9.1	-120°C	**176**	**86***	0
B2	BGK9.2	-130°C	82	59	1
B2	BGK9.3	-130°C	95	67	1
B2	BGK9.4	-130°C	91	64	1
B2	BGN9.1	-100°C	**313**	**97***	0
B2	BGN9.2	-140°C	100	70	1
B2	BGN9.3	-140°C	107	75	1
B2	BGN9.4	-120°C	108	75	1
B2	BGK4.1	-130°C	63	47	1
B2	BGJ7.1	-140°C	78	56	1
B2	BGJ7.2	-130°C	52	40	1
B2	BGQ5.1	-140°C	53	41	1
B2	BGQ5.2	-140°C	85	61	1
R4	156 B	-100°C	**148**	**93***	0
R4	156 C	-100°C	88	63	1
R4	156 E	-100°C	76	55	1
R4	156 H	-100°C	72	52	1
R4	156 I	-100°C	104	73	1
R4	224.1	-130°C	71	52	1
R4	224.2	-130°C	87	62	1
R4	224.3	-130°C	46	36	1
R4	224.4	-120°C	43	34	1
R4	224.5	-120°C	64	47	1
R4	224.6	-80°C	**213**	**91***	0
R4	224.7	-120°C	78	56	1
R4	224.8	-110°C	59	44	1
R4	224.9	-90°C	126	87	1

R4	224.10	-100°C	55	42	1
R4	230 A	-100°C	61	46	1

$K_{Jc\text{-}4mm}$ = K_{Jc} value measured with the tested miniature specimen
$K_{Jc\text{-}25mm}$ = K_{Jc} value size corrected to 25 mm specimen size
δ = 1 test ended with cleavage fracture
δ = 0 test ended in ductile fracture mode
* $K_{Jc\ (limit)}$ value used in determination of T_0

Values **in bold purple** indicate that the validity criteria defined in ASTM E1921 standard were exceeded. The criteria are: $K_{Jc} < K_{Jc\ (limit)}$ and Δa_{stable} < minimum (0, 05*(W-a_0) or 1 mm, whichever is smaller) at the onset of cleavage fracture.

The determination of the transition temperature T_0 of Barsebäck 2 material and Ringhals 4 surrogate weld metal was done by iteration (see Eq. 12), since tests were executed at multiple temperatures instead of single temperature. All specimens K_{Jc} data was converted to correspond the standard 1T specimen to ensure acceptance and comparison of the results. Based on the previous CVN results, the initial test temperature was determined as -120°C and tests were carried out between -80°C to -140°C.

The Master Curves for studied Barsebäck 2 material and Ringhals 4 surrogate weld metal are presented in Figures 61 and 62; in order for the specimen test data to be applicable in the Master Curve adaption, it must fit within allowable temperature range; ASTM E1921 determines such range to be $T_0 \pm 50°C$.

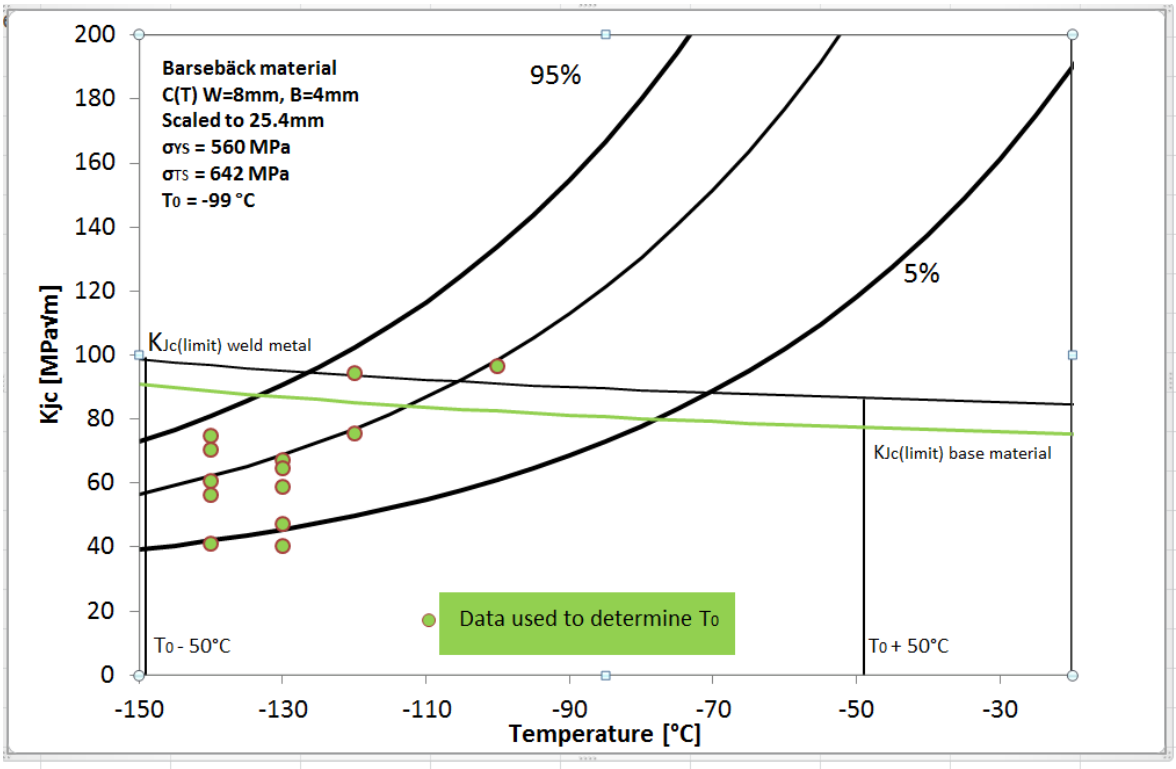

Figure 61 Master Curve of Barsebäck 2 material.

For the Barsebäck 2 material, T_0 is -99 °C and the test data settles between allowable ranges; thus, all data is applicable. Two data points exceeded the $K_{Jc(limit)}$ and therefore these points were treated as censored data at the iteration phase in the determination of T_0. The lower $K_{Jc(limit)}$ (in green) indicates the limit calculated with σ_{YS} of the base material. The upper $K_{Jc(limit)}$ was calculated with σ_{YS} of the weld metal and it holds true for specimens with consistency of HAZ also, since the hardness values were in the same region.

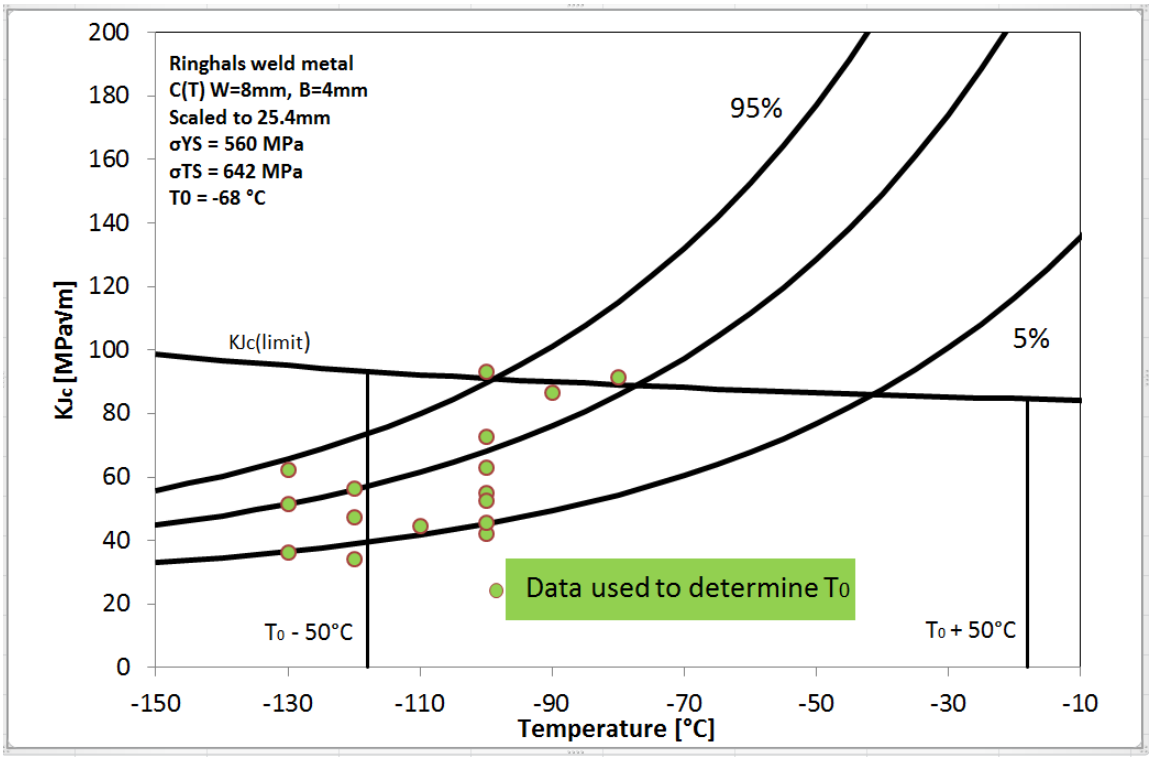

Figure 62 Master Curve of Ringhals 4 surrogate weld metal.

For the Ringhals 4 surrogate weld metal, T_0 is -68°C. Since T_0 is relatively high in contrast to test temperatures, six data points exceeded the lower limit of allowable temperature range. Additionally, two data points exceeded the $K_{Jc(limit)}$ and similarly as with the two exceeding data points in Barsebäck 2 material, these data points were also treated as censored data in the iteration phase.

T_0 for Ringhals 4 surrogate weld metal is determined with all data points even if some data points exceed the T_0 ±50°C criteria. ASTM E1921 gives further clarification for the case where data point does not meet the allowable temperature range ± 50°C; the oscillation iteration phenomenon between distinct T_{0Q} values will likely be resolved with more testing near the T_{0Q} values.

6 Discussion

6.1 Initiation location and fractography

Cleavage fracture tends to initiate near the maximum stress location when the stress preceding the crack tip exceeds the critical fracture stress σ_f, see Figure 18. The location of critical fracture stress respective to fatigue pre-crack can be estimated with Eq.17. Equation 18 shows formula for calculating factor m. The distance of the maximum stress from the fatigue pre-crack tip is approximately 2δ (2 times crack-tip-opening displacement). Table 13 shows the data used for calculation of the location of maximum stress and Table 14 shows 2δ results, the location of maximum stress. When calculating the 2δ, the used J value was the value at the onset of cleavage fracture, J_c, determined for the original specimen. Moreover, σ_{YS} was corrected as in Eq. 14 to correspond the test temperature of each specimen.

$$2\delta = 2 \times \left(\frac{J}{m\,\sigma_Y}\right) \tag{17}$$

where:

2δ	is the distance of maximum stress from the fatigue pre-crack tip [mm]
δ	is crack-tip-opening displacement [mm]
J	is J-integral
m	is constraint factor
σ_Y	is yield strength [MPa]

$$m = A_0 - A_1 \times \left(\frac{\sigma_{YS}}{\sigma_{TS}}\right) + A_2 \times \left(\frac{\sigma_{YS}}{\sigma_{TS}}\right)^2 - A_3 \times \left(\frac{\sigma_{YS}}{\sigma_{TS}}\right)^3 \tag{18}$$

where:

σ_{YS}	is yield strength [MPa]
σ_{TS}	is tensile strength [MPa]
A_0	is 3.18 - 0.22 × (a_0/W)
A_1	is 4.32 - 2.23 × (a_0/W)
A_2	is 4.44 - 2.29 × (a_0/W)
A_3	is 2.05 – 1.06 × (a_0/W)

Table 13. Data used to calculate the location of the maximum stress.

Specimen	σ_{YS} [MPa]	σ_{TS} [MPa]	J [MJ]	m
BGK9.1	600	730	0.134721	1.863
BGK9.2	625	747	0.028922	1.824
BGK9.3	760	838	0.039284	1.768
BGK9.4	760	838	0.035630	1.768
BGN9.2	789	858	0.043496	1.748
BGN9.3	654	765	0.049501	1.829
BGN9.4	600	730	0.050836	1.850
BGQ5.1	789	858	0.012316	1.770
BGQ5.2	654	765	0.032607	1.808
BGJ7.1	654	765	0.026191	1.815
BGJ7.2	760	838	0.011659	1.768

σ_{YS} = temperature corrected yield strength [MPa]
σ_{TS} = temperature corrected ultimate tensile strength [MPa]
J = J-integral value at the onset of cleavage fracture [MJ]
m = constraint factor

Table 14. Approximate location of the maximum stress.

Specimen	2δ [mm]
BGK9.1	0.238
BGK9.2	0.054
BGK9.3	0.074
BGK9.4	0.069
BGN9.2	0.085
BGN9.3	0.085
BGN9.4	0.094
BGQ5.1	0.024
BGQ5.2	0.066
BGJ7.1	0.049
BGJ7.2	0.022

Figure 63 shows the measured location of crack initiation site (Table 9) and the calculated location of maximum stress ahead of the fatigue pre-crack tip obtained for Barsebäck 2 material.

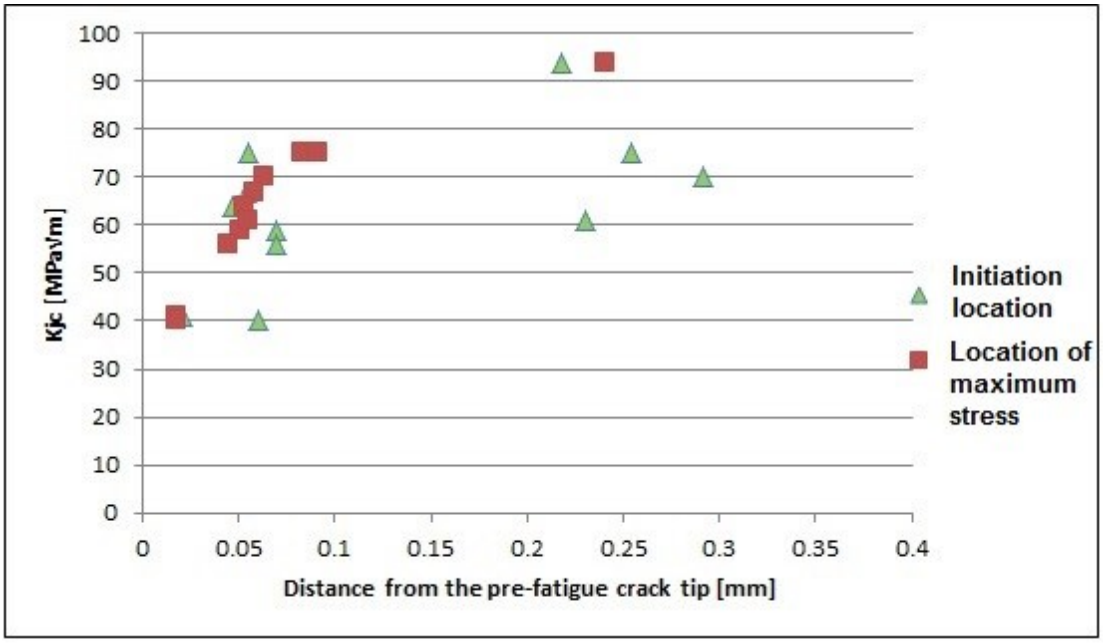

Figure 63 Locations of crack initiation sites and maximum stresses of Barsebäck 2 material.

As can be seen from Figure 63, results obtained are very similar to what earlier studies prove; crack tends to initiate near the maximum stress site (Anderson, 2005). Also, there is a correlation between increasing fracture toughness and growing distance between initiation site and the fatigue pre-crack tip.

Figure 63 and Table 14 indicate that the majority of crack initiations evidently occurred near the maximum stress location; however, three individual crack initiation sites located relatively far from the maximum stress site. Such location is interesting and contrary to scientific knowledge. A possible reason may be the fact that qualitative determination of the crack initiation location through SEM is challenging. Additionally, the estimation formula for the location of the maximum stress, Eq. 17, is approximate. A more accurate location for the maximum stress can be obtained with the finite element method.

The following features are characteristic when the fracture is brittle:

- cleavage planes
- cleavage steps
- cleavage facets
- river patterns

All above-mentioned features were observed in the SEM images. It is not unusual that though fracture mode is brittle, there may be signs characteristic to ductile fracture in the fracture surface and such signs appeared in some specimen fracture surfaces. This is

common particularly in the transition region. In the ductile-brittle transition range some specimens may act ductile and some specimens brittle in the same assessment temperature regardless of being made from the same material. Regardless of differences in test temperature and fracture toughness level, clear majority of specimen showed typical cleavage fracture.

6.2 Applicability of T_0 determined with miniature C(T) specimens

A major question regarding miniature C(T) specimens is whether the usage of miniature sized C(T) specimens is applicable when determining fracture toughness of weld metals in the ductile-brittle transition range. Down-sized specimens cause reasonable doubts concerning the validity of fracture toughness; a reduced size may give elevated material toughness values. The present ASTM standards give requirements about the specimen size, and ASTM E1921 allows the usage of miniature size specimens which is a valuable matter, since determination of the transition temperature in the ductile-brittle transition range of a small material volume is crucial in the surveillance programs of operating NPPs.

Studies have been made regarding the applicability of miniature C(T) specimens in fracture toughness determination with homogeneous materials (Wallin et al., 2016; Yamamoto et al., 2015), some with weld metals (Yamamoto and Miura, 2015; Sokolov, 2017) and also with irradiated materials (Yamamoto, 2017; Ha et al., 2017). Findings prove that:

- The miniature size by definition has no significant effect neither to determination of fracture toughness nor transition temperature T_0.

- The geometry of sub-size C(T) specimen is usable and manufacturing of specimens is feasible without any additional arrangements regarding machining.

- Side-grooving has no notable influence to fracture toughness outcomes.

- For the Master Curve evaluation, the weld metal is as acceptable as the base material.

- The reuse of tested CVN specimens is very useful in general but exceptionally useful with irradiated materials when availability is limited.

- No inaccuracy or inconsistencies were found in determination of the transition temperature T_0.

Outcome of the studies in this thesis followed abovementioned findings; K_{Jc} values were consistent despite non-side-grooved specimens. From three whole and five CVN specimen halves 53 miniature C(T) specimens were manufactured and T_0 was determined successfully.

The transition temperatures T_0 in ductile-brittle transition range obtained with the Master Curve adaptation in this study were:

- Barsebäck 2 material, -99°C
- Ringhals 4 surrogate weld metal, -68°C

Observe, though, that the Barsebäck 2 curve is based on a mixture of specimens containing weld metal, HAZ or base material.

Experimental results from the surveillance programmes of Ringhals 3 and 4 NPPs, with similar chemical composition as Barsebäck 2 material (May et al., 2015), give T_0 for unirradiated Ringhals 4 weld metal and weld metal obtained from the replaced Ringhals RPV head as following:

- Ringhals 4 WM, -125°C
- Pressure vessel head WM, -97°C

The Ringhals results were obtained with 5 mm and 10 mm thick specimens. Since the above Ringhals results and the T_0 for Barsebäck 2 material are in the same range, the miniature C(T) specimens give a reliable T_0 value despite the smaller size. The results indicate that the miniature sized C(T) specimens are applicable for determination of T_0 of the Barsebäck 2 material. Regarding the Ringhals 4 surrogate material, a possible cause for relatively large difference to earlier experimental values is that the weld was made of surrogate weld material. However, T_0 values of Barsebäck 2 material and Ringhals 4 surrogate weld metal are low and it is improbable that cleavage fracture will occur at room temperature.

With Ringhals 4 surrogate weld metal from this study the distribution of data points was more dispersed; six data points were left out from allowable temperature range ± 50°C. A conceivable resolution for this would have been to determine T_0 excluding these six data points and to obtain a bit lower T_0, but then again, the allowable temperature range would have moved to more lower direction and formerly excluded data points would now fit inside the allowable temperature range. Hence, the T_0 was determined including all data points.

6.2.1 Microstructure of Barsebäck 2 material

The microstructure of the tested specimens from Barsebäck 2 material was unexpected; microstructural examinations revealed that the consistency obtained was not weld metal by default, but composite of three different microstructures: base material, heat affected zone and weld metal. This may be as a consequence of relatively narrow weld of the Barsebäck 2 material from where the CVN specimens were cut originally. The notch of the CVN specimen may well have located in the weld metal, and the miniature C(T) specimen cut from tested halves of the CVN specimen was no longer in the weld metal but in the base material or in the heat affected zone. Macroetching of the CVN specimens before cutting would have revealed this.

6.3 Future work

The characterization of the Barsebäck material continues in BREDA project. In BREDA collaboration is done between Finnish and Swedish institutions. The main goal is to estimate how well the surveillance programme describes the ageing behavior of reactor pressure vessel. In BREDA, Barsebäck Research & Development Arena, samples are harvested from Barsebäck (Sweden) reactor pressure vessel. The fracture mechanical properties of the RPV samples are compared to the existing results from surveillance

programme of Barsebäck. The experimental investigations focus on the weld, as the weld materials are the limiting materials from the Long Term Operation, LTO, perspective.

7 Conclusions

The monitoring of RPV steels is an operational precondition of NPP technology and the utmost important matter. The RPV is made from bainite-ferrite steel which has an increasing tendency to brittle behaviour under irradiation; irradiation also causes rising of the ductile-brittle transition temperature and hence the long-term surveillance is needed. The surveillance programs are based on observing changes in the mechanical properties of life-limiting structural materials and establish the need for reference material. Test data obtained from the reference material gives an early estimate of any degradation of mechanical properties.

Availability of the reference material is limited and therefore the applicability of miniature size C(T) specimens is of great interest. Surveillance tested CVN specimen halves enable manufacturing of miniature size C(T) specimens not only in the perspective of financial savings but also on account of the fact that ASTM E1921 allows the use of sub-size specimens in the determination of transition temperature T_0. However, fracture toughness can be size dependent and consequently; the applicability of miniature size specimens needs to be verified for the reliability and accuracy of the test results obtained from testing of weld metals.

Fracture mechanics concepts including ductile and brittle fracture, the Master Curve theory and delineation of standards ASTM E1820 and ASTM E1921 were introduced with scientific literature review. Moreover, RPV materials and manufacturing were portrayed and metallographic characterisation was outlined. An experimental investigation was carried out to determine the transition temperature T_0 of the two materials studied; Barsebäck 2 material and Ringhals 4 surrogate weld metal. Barsebäck 2 material was a pressure vessel surveillance weld from core region, whereas Ringhals 4 surrogate weld metal was a surrogate weld of the pressure vessel head. The hardness and initial crack lengths were measured, and additionally fracture surfaces and microstructures were characterised. An unexpected inconsistency of Barsebäck 2 material was revealed in microstructural examinations. It was observed that mini C(T) specimens contained weld metal, HAZ and base material instead of being weld metal as presumed.

Crack initiation sites were determined qualitatively; the location of crack initiation site was measured by SEM and the site of maximum stress ahead of the fatigue pre-crack tip was calculated. The results obtained in this thesis were similar, and indicate that the cracks are prone to initiate near the maximum stress region. Additionally, a correlation between increasing fracture toughness and growing distance between initiation site and the fatigue pre-crack tip was observed; in accordance to earlier studies.

Regardless of some exceeding of data points, the transition temperature T_0 was determined with all data points for both Barsebäck 2 material and Ringhals 4 surrogate weld metal, and the transition temperatures T_0 were:

- Barsebäck 2 material, -99°C

- Ringhals 4 surrogate weld metal, -68°C

Prior experimental results obtained with larger specimens from the surveillance programmes of Ringhals 3 and Ringhals 4 NPPs, with similar chemical compositions as Barsebäck 2 material were in the same range as the T_0 of Barsebäck 2 material. Hence, in spite of the smaller size and the abrupt microstructure, the miniature C(T) specimens give a reliable T_0 value and the applicability for determination of T_0 is possible.

References

American Nuclear Society. (2012), ANS Nuclear cafe, [Accessed 04/23/2017], Available at: http://ansnuclearcafe.org/2012/08/15/doel-3-rpv/#sthash.kiZLdpdr.dpbs.

Anderson, T.L. (2005), *Fracture Mechanics Fundamentals and Applications*, 3rd ed., CRC Press Taylor & Francis Group, USA, ISBN 978-1-4200-5821-5.

Anderson, T.L. and Dodds, R.H. (1993), Simple constraint corrections for subsize fracture toughness specimens, *Small Specimen Test Techniques Applied to Nuclear Reactor Vessel Thermal Annealing and Plant Life Extension, ASTM STP 1204*, ASTM International, USA, pp. 93–105, ISBN 0803118694.

Ando, Y. (1980), Forgings for pressurised components of a nuclear steam supply, in Nichols, R.W. (Ed.), *Developments in Pressure Vessel Technology - 3*, Applied Science Publisher LTD, UK, pp. 35–59.

AREVA. (2017), Irradiation surveillance program to support the RPV materials assessment, [Accessed 03/26/2017], Available at: http://de.areva.com/customer/liblocal/docs/KUNDENPORTAL/Forward Alliance Katalog/Aging Management by Component/F-007_RPV-Surveillance-Program.pdf.

ASME. (2017), Boiler and pressure vessel code, 2017 Edition, [Accessed 08/29/2017], Available at: https://www.asme.org/shop/standards/new-releases/boiler-pressure-vessel-code-2013.

ASTM E1820. (2015), *E1820: Standard Test Method for Measurement of Fracture Toughness*, ASTM International, USA, pp. 1–54.

ASTM E1921. (2015), *E1921: Standard Test Method for Determination of Reference Temperature, T_0, for Ferritic Steels in the Transition Range*, ASTM International, USA, pp. 1–23.

Bhadeshia, H. and Honeycombe, R. (2006), The embrittlement and fracture of steels, in Bhadeshia, H. and Honeycombe, R. (Eds.), *Steels: Microstructure and Properties*, 2nd ed., Elsevier, pp. 303–341, ISBN 978-0-7506-8084-4.

Blagoeva, D.T., Debarberis, L., Jong, M. and Pierick, P. (2014), Stability of ferritic steel to higher doses: Survey of reactor pressure vessel steel data and comparison with candidate materials for future nuclear systems, *International Journal of Pressure Vessels and Piping*, Vol. 122, pp. 1–5.

Callister, W.D. (2007), *Materials Science and Engineering*, 7th ed., John Wiley & Sons, Inc., USA, ISBN 978-0-471-73696-7.

Campbell, F.C. (2008), *Elements of Metallurgy and Engineering Alloys*, ASM International, ISBN 9781680159608.

Campbell, F.C. (2012), Ductile and brittle fracture, in Campbell, F.C. (Ed.), *Fatigue and Fracture - Understanding the Basics*, ASM International, pp. 55–100, ISBN 978-1-62198-373-6.

Cary, H.B. and Helzer, S.C. (2005), *Modern Welding Technology*, 6th ed., Pearson Education, Inc., USA, ISBN 0-13-113029-3.

Chen, Z.A., Zeng, Z. and Chao, Y.J. (2007), Effect of crack depth on the shift of the ductile-brittle transition curve of steels, *Engineering Fracture Mechanics*, Vol. 74, No. 15, pp. 2437–2448.

Curry, D.A. and Knott, J.F. (1979), Effect of microstructure on cleavage fracture toughness of quenched and tempered steels, *Metal Science*, Vol. 13, No. 6, pp. 341–345.

Engel, L. and Klingele, H. (1981), *An Atlas of Metal Damage*, Wolfe Publishing Ltd, UK, ISBN 0723407509.

English, C. and Hyde, J. (2012), Radiation damage of reactor pressure vessel steels, in Hashmi, S. (Ed.), *Comprehensive Nuclear Materials*, 4th ed., Elsevier, pp. 151–180.

Epsilon Tech. (2017), Fracture mechanics clip-on gages, [Accessed 04/27/2017], Available at: http://www.epsilontech.com/wp-content/uploads/product-specs/3541.pdf.

Eyres, D.J. and Bruce, G.J. (2012), *Ship Construction*, 7th ed., Elsevier Science, ISBN 9780080972398.

Ha, Y., Tobita, T., Takamizawa, H. and Nishiyama, Y. (2017), Fracture toughness evaluation of neutron-irradiated reactor pressure vessel steel using miniature-C(T) specimens, *Proceedings of the ASME 2017 Pressure Vessels and Piping Conference, July 16-20, 2017, Waikoloa, Hawaii, USA*, PVP2017-65568, pp. 1–5.

Hamilton, I.G. (1980), Ferritic steel plates for pressure vessels, in Nichols, R.W. (Ed.), *Developments in Pressure Vessel Technology - 3*, Applied Science Publisher LTD, UK, pp. 1–33.

Haušild, P., Siegl, J., Materna, A., Kytka, M. and Kopřiva, R. (2016), Characterization of reactor pressure vessel steel by ABI testing, *Procedia Materials Science*, Vol. 12, pp. 7–11.

Hertzberg, R.W., Vinci, R.P. and Hertzberg, J.L. (2013), *Deformation and Fracture Mechanics of Engineering Materials*, 5th ed., John Wiley & Sons, Inc., USA, ISBN 978-0-470-52780-1.

IAEA-TECDOC-1631. (2009), *Master Curve Approach to Monitor Fracture Touhgness of Reactor Pressure Vessels*, Vienna, ISBN 9789201110091.

Japan Atomic Energy Agency. (2017), Japan Atomic Energy Agency Nuclear Safety Research Center (NSRC), [Accessed 03/26/2017], Available at: http://www.jaea.go.jp/04/anzen/en/group/mwcrg/index_e.html.

Kocak, M., Webster, S., Janosch, J., Ainsworth, R. and Koers, R. (2008), *FITNET - Fitnes for Service- Fracture, Fatigue, Creep, Corrosion*, 1st ed., Germany.

Kou, S. (2003), *Welding Metallurgy*, 2nd., John Wiley & Sons, Inc., USA, ISBN 978-0-471-43491-7.

Krauss, G. (2015), Deformation, strengthening, and fracture of ferritic microstructures, in Krauss, G. (Ed.), *Steels - Processing, Structure, and Performance*, 2nd ed., ASM International, pp. 213–232, ISBN 978-1-62708-083-5.

Liu, A. (2005), Deformation and fracture mechanisms and static strength of metals, in Liu, A. (Ed.), *Mechanics and Mechanism of Fracture: An Introduction*, ASM International, pp. 47–119, ISBN 978-1-5231-0207-5.

Lydman, J., Nevasmaa, P. and Ehrsten, U. (2017), Microstructural characterization of non-irradiated Barsebäck RPV material, *Research Report VTT-R-05554-17*, Espoo.

May, J., Rouden, J., Efsing, P., Valo, M. and Hein, H. (2015), Extended mechanical testing of RPV surveillance materials using reconstitution technique for small sized specimen to assist long term operation, in Sokolov, M., Lucon, E. (Ed.), *Small Specimen Test Techniques: 6th Volume*, ASTM International, USA, pp. 88–109.

McCabe, D., Merkle, J. and Wallin, K. (2005), *An Introduction to the Development and Use of the Master Curve Method*, ASTM International, USA, ISBN 0-8031-3368-5.

Miekkoja, H.K. (1965), *Metallioppi*, 3rd ed., Teknillisten Tieteiden Akatemia, Otava, Helsinki.

Odette, G.R. and Lucas, G.E. (2001), Embrittlement of nuclear reactor pressure vessels, *JOM Journal of the Minerals Metals and Materials Society*, Vol. 53, No. July, pp. 18–22.

Planman, T. and Server, W.L. (2012), Fracture toughness master curve of bcc steels, in Hashmi, S. (Ed.), *Comprehensive Nuclear Materials*, 4th ed., Elsevier Inc., pp. 433–461, ISBN 9780080560335.

Ritchie, R.O., Knott, J.F. and Rice, J.R. (1973), On the relationship between critical tensile stress and fracture toughness in mild steel, *Journal of the Mechanics and Physics of Solids*, Vol. 21, No. 6, pp. 395–410.

Rogerson, J.H. (1980), Welding defects and their elimination, in Nichols, R.W. (Ed.), *Developments in Pressure Vessel Technology - 3*, Applied Science Publisher LTD,

UK, pp. 327–355.

Server, W.L., Nanstad, R.K. and Odette, G.R. (2017), Use of reactor pressure vessel surveillance materials for extended life evaluations using power and test reactor irradiations, [Accessed 03/26/2017], Available at: http://www.iaea.org/inis/collection/NCLCollectionStore/_Public/43/070/43070853.pdf.

SFS Standards Publication. (2012), *SFS-EN ISO 643:2012 Steels — Micrographic Determination of the Apparent Grain Size*, Suomen Standardisoimisliitto SFS, Helsinki, pp. 1–46.

Shen, M., Peng, X., Xie, L., Meng, X. and Li, X. (2016), Deformation characteristics and sealing performance of metallic o-rings for a reactor pressure vessel, *Nuclear Engineering and Technology*, Elsevier B.V, Vol. 48, No. 2, pp. 533–544.

Smallman, R.E. and Ngan, A.H.W. (2007), *Physical Metallurgy and Advanced Materials*, 7th ed., Elsevier, ISBN 978-0-7506-6906-1.

Sokolov, M. (2017), Use of mini-CT specimens for fracture toughness characterization of low upper-shelf linde 80 weld, *Proceedings of the ASME 2017 Pressure Vessels and Piping Conference, July 16-20, 2017, Waikoloa, Hawaii, USA*, PVP2017-65904, pp. 1–4.

Soneda, N. (2015), *Irradiation Embrittlement of Reactor Pressure Vessels (RPVs) in Nuclear Power Plants*, Elsevier, ISBN 9780857096470.

Sonsino, C.M. (2009), Effect of residual stresses on the fatigue behaviour of welded joints depending on loading conditions and weld geometry, *International Journal of Fatigue*, Vol. 31, No. 1, pp. 88–101.

Stec, M. and Faleskog, J. (2009), Micromechanical modeling of grain boundary resistance to cleavage crack propagation in ferritic steels, *International Journal of Fracture*, Vol. 160, No. 2, pp. 151–167.

Wallin, K. (2017), Research Professor, VTT, Espoo, Finland, E-mail, 3.11.2017.

Wallin, K., Planman, T., Valo, M. and Rintamaa, R. (2001), Applicability of miniature size bend specimens to determine the master curve reference temperature To, *Engineering Fracture Mechanics*, Vol. 68, No. 11, pp. 1265–1296, ISBN 0013-7944.

Wallin, K., Yamamoto, M. and Ehrnsten, U. (2016), Location of initiation sites in fracture toughness testing specimens -the effect of size and side grooves, *Proceedings of the ASME 2016 Pressure Vessels and Piping Conference, July 17-21, 2016, Vancouver, British Columbia, Canada*, PVP2016-63078, pp. 1–9.

World Nuclear Association. (2017), Nuclear power in Sweden, [Accessed 08/20/2017], Available at: http://www.world-nuclear.org/information-library/country-profiles/countries-o-s/sweden.aspx.

Yamamoto, E., Shiga, K., Kayano, R., Okazaki, T., Watanabe, H., Kiso, T., Tahara, T., et al. (2013), Guidelines for repair welding of pressure equipment in refineries and chemical plants, *Journal of Pressure Vessel Technology*, Vol. 135, No. 3, pp. 1–12.

Yamamoto, M. (2017), The Master Curve fracture toughness evaluation of irradiated plate material JRQ using miniature-C(T) specimens, *Proceedings of the ASME 2017 Pressure Vessels and Piping Conference, July 16-20, 2017, Waikoloa, Hawaii, USA*, PVP2017-66085, pp. 1–8.

Yamamoto, M. and Miura, N. (2015), Applicability of miniature C(T) specimens for the Master Curve evaluation of RPV weld metal, *Proceedings of the ASME 2015 Pressure Vessels and Piping Conference, July 19-23, 2015, Boston, Massachusetts, USA*, pp. 1–7, ISBN 9780791856925.

Yamamoto, M., Onizawa, K., Yoshimoto, K., Ogawa, T., Mabuchi, Y., Valo, M., Lambrecht, M., et al. (2015), International round robin test on Master Curve reference temperature evaluation utilizing miniature C(T) specimen, *ASTM Special Technical Publication*, Vol. STP 1576, ASTM International, USA, pp. 53–69, ISBN 9780803175976.

Appendix A, Test report

ASTM E1921-15 standard test to determine reference temperature T_0
Specimen BGK9 sauva 3

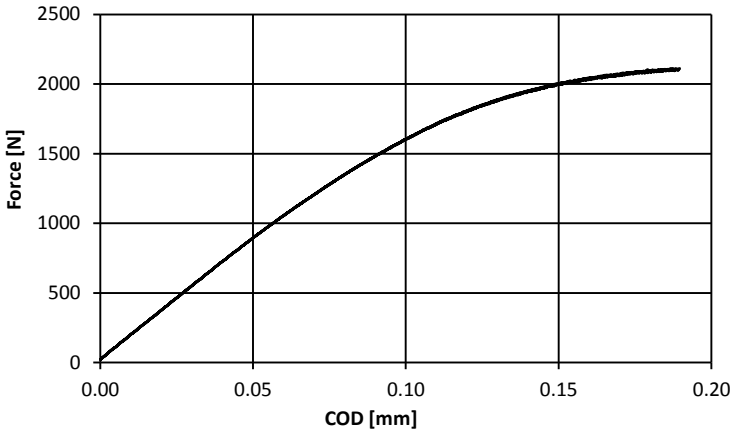

Material

Barsebäck 2 material

$R_{p0,2\ (RT)}$	560	MPa
$R_{m\ (RT)}$	642	MPa

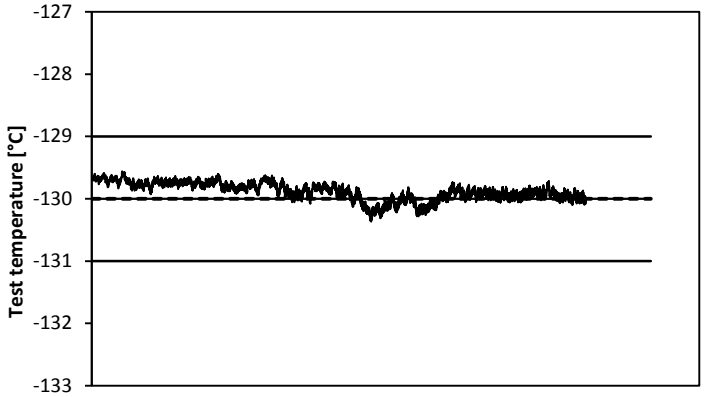

Specimen

Specimen name	BGK9 sauva 3
Specimen orientation	
Specimen type	C(T)
Specimen thickness, B [mm]	3.96
Specimen net thickness, B_N [mm]	3.96
Specimen width, W [mm]	8.07
Precrack length, a_0 [mm]	4.39
Stable crack growth, Δa [mm]	

Test

Pop-in, C_i/C_0	no
Displacement measurement	front face
K_{max} for final 0,64 mm of fatigue precracking [MPa√m]	13.87
Test temperature, T [°C]	-130
Plastic area, A_p [Nm]	0.133
Fracture toughness K_{Jc} [MPa√m]	95.2

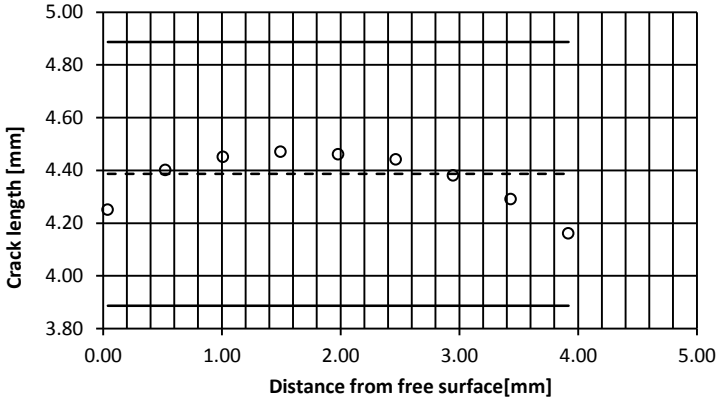

Crack length

	Distance from free surface [mm]	Precrack length [mm]	Final crack length [mm]	Qualification according to 8.9.1
a_i				
a_1	0.04	4.25		OK
a_2	0.53	4.40		OK
a_3	1.01	4.45		OK
a_4	1.50	4.47		OK
a_5	1.98	4.46		OK
a_6	2.46	4.44		OK

a_7	2.95	4.38		OK
a_8	3.43	4.29		OK
a_9	3.92	4.16		OK
average		a_0= 4.39	a_f=	
$(a_{i,max}-a_{i,min})/a$ [%]		7.1		

Qualification of data

8.9.1	a_i-a_0 < maximum (0,05*B, 0,5 mm)	OK
8.9.2	● measurement capacity: $K_{JC} < K_{JC(limit)}$	OK
	● crack growth validity: Δa_{stable} < minimum (0,05*(W-a_0), 1 mm) at the onset of cleavage fracture	OK
8.9.3	cleavage fracture	OK